JGR Oceans

RESEARCH ARTICLE
10.1029/2023JC020422

Defining Mesoscale Eddies Boundaries From In-Situ Data and a Theoretical Framework

Yan Barabinot[1], **Sabrina Speich**[1], **and Xavier Carton**[2]

[1]Ecole Normale Supérieure, Laboratoire de Météorologie Dynamique (LMD), Paris, France, [2]Laboratoire d'Océanographie Physique et Spatiale (LOPS), Université de Bretagne Occidentale (UBO), IUEM, Plouzané, France

Abstract Mesoscale eddies play an important role in transporting water properties, enhancing air-sea interactions, and promoting large-scale mixing of the ocean. They are generally referred to as "coherent" structures because they are organized, rotating fluid elements that propagate within the ocean and have long lifetimes (months or even years). Eddies have been sampled by sparse *in-situ* vertical profiles, but because *in-situ* ocean observations are limited, they have been characterized primarily from satellite observations, numerical simulations, or relatively idealized geophysical fluid dynamics methods. However, each of these approaches has its limitations. Many questions about the general structure and "coherence" of ocean eddies remain unanswered. In this study, we investigate the properties of seven mesoscale eddies sampled with relative accuracy during four different field experiments in the Atlantic. Our results suggest that the Ertel Potential Vorticity (EPV) is a suitable parameter to isolate and characterize the eddy cores and their boundaries. The latter appear as regions of finite horizontal extent, characterized by a local extremum of the vertical and horizontal components of the EPV. These are found to be closely related to the presence of a different water mass in the core (relative to the background) and the steepening of the isopycnals due to eddy occurrence and dynamics. Based on these results, we propose a new criterion for defining eddies at the mesoscale. We test our approach using a theoretical framework and explore the possible magnitude of this new criterion, including its upper bound.

Plain Language Summary Mesoscale eddies are ubiquitous rotating currents in the ocean. They are considered as one of the most important sources of ocean variability because they can live for months and transport and mix heat, salt, and other properties within and between ocean basins. They have been studied extensively from satellite observations because they are often at or near the ocean surface. However, observations of their 3D structure are rare, and calculations of eddy transport are often approximated without precise knowledge of their true vertical extent. In addition, recent studies suggest the existence of subsurface eddies that are not detectable from satellite observations. Here, we characterize and attempt to generalize 3D eddy properties by analyzing observations collected during specific high-resolution field experiments in the Atlantic Ocean. We also propose a criterion, based on geophysical fluid dynamics theory, that defines the lateral and vertical eddy boundaries. This criterion can be applied broadly to assess eddy structure, volume, transport, and evolution more quantitatively than in previous studies. We also provide insight into why these boundaries are substantial, which may explain why oceanic eddies are coherent structures that can span long distances and have long lifetimes.

Key Points:

- A new criterion that compare the horizontal and vertical components of Ertel PV is introduced to characterize eddies boundaries
- Eddy boundaries behave like a front
- The Rossby number and the vertical stratification anomaly drive eddies boundaries intensity

Supporting Information:

Supporting Information may be found in the online version of this article.

Correspondence to:

Y. Barabinot,
yan.barabinot@ens-paris-saclay.fr

Citation:

Barabinot, Y., Speich, S., & Carton, X. (2024). Defining mesoscale eddies boundaries from in-situ data and a theoretical framework. *Journal of Geophysical Research: Oceans*, *129*, e2023JC020422. https://doi.org/10.1029/2023JC020422

Received 1 SEP 2023
Accepted 15 JAN 2024

Author Contributions:

Conceptualization: Yan Barabinot, Sabrina Speich, Xavier Carton
Formal analysis: Yan Barabinot, Sabrina Speich, Xavier Carton
Funding acquisition: Sabrina Speich, Xavier Carton
Investigation: Yan Barabinot
Methodology: Yan Barabinot, Sabrina Speich, Xavier Carton
Project administration: Yan Barabinot
Resources: Sabrina Speich, Xavier Carton
Supervision: Sabrina Speich, Xavier Carton
Validation: Yan Barabinot, Sabrina Speich, Xavier Carton
Visualization: Yan Barabinot
Writing – original draft: Yan Barabinot
Writing – review & editing: Sabrina Speich, Xavier Carton

1. Introduction

Mesoscale eddies are ubiquitous in the ocean and have been observed by satellite and sparse *in-situ* measurements for several decades. They are defined as relatively long-lived horizontal recirculations of seawater on a spatial scale close to one or a few deformation radii and smaller than the Rhines scale (Rhines, 1975). Since the 1990s, satellite observations (mainly altimetry) have been used to detect mesoscale eddies in the ocean and to assess their intensity, lifetime, and trajectories (Chaigneau et al., 2009; Chelton et al., 2011). The number, lifespan, and structure of mesoscale eddies have also been investigated using surface drifters (Lumpkin, 2016), acoustically tracked floats (Richardson & Tychensky, 1998), or Argo vertical profiling floats ((Laxenaire et al., 2019, 2020; Nencioli et al., 2016), as well as moorings and shipboard observations (e.g., Barceló-Llull et al., 2017; Z. Zhang et al., 2016). This lifetime often exceeds several months and can reach several years (Ioannou et al., 2022; Laxenaire et al., 2018). Such longevity suggests that most mesoscale eddies in the ocean are resilient dynamical structures.

One of the most important properties of mesoscale eddies is their ability to trap water masses at their source and transport them over very long times and distances. In fact, due to their quasi-2D recirculating fluid motions, water masses in the eddy core remain constrained by closed trajectories created by the azimuthal velocity field. This phenomenon was first described by Flierl (1981) when surface drifters and subsurface floats became an important tool for measuring ocean processes. Using a Lagrangian approach, he proposed that if the eddy azimuthal mean velocity field is greater than the translational velocity, then fluid particles are trapped in the core of the eddy. As a result, the water masses in the eddy core often differ from the surrounding water masses and are thus associated with temperature/salinity anomalies (e.g., Ioannou et al., 2022; L'Hégaret, Carton, et al., 2015; L'Hégaret, Duarte, et al., 2015; Laxenaire et al., 2019, 2020).

Therefore, mesoscale eddies are thought to play an important role in the transport of properties (heat, salt, carbon, and other chemical constituents) as they propagate through the ocean, representing a key dynamic element in the overall global budget of these tracers (Bryden, 1979; Jayne & Marotzke, 2002; Morrow & Traon, 2012; Wunsch, 1999). In addition, mesoscale eddies influence several ocean processes, from air-sea fluxes (Frenger et al., 2013), to ventilation of the ocean interior (Sallée et al., 2010), to large-scale ocean circulation (Lozier, 1997; Morrow et al., 1994). Due to temperature/salinity differences between the water masses trapped inside and outside the eddies, the eddy boundaries have often been characterized as large gradients in thermohaline properties, resulting in finite gradient regions (Pinot et al., 1995; Martin et al., 2002; J. Chen et al., 2020). There the variance increases and it can be assumed that the diffusion of the tracer also increases (Hua & Klein, 1998; Lapeyre et al., 2001; Sobel et al., 1997). However, even in the case of turbulent diffusion, this process is very slow in the ocean (turbulent diffusion coefficients are on the order of 10^{-4} m^2/s vertically and $1-10$ m^2/s horizontally (Bowden, 1965; Nencioli et al., 2013). Ruddick and Gargett (2003) and Ruddick et al. (2010) showed that for axisymmetric Mediterranean eddies (or Meddies), lateral mixing is mostly generated by lateral intrusions. In these studies, the horizontal diffusion coefficient due to these intrusions was estimated to be between 1 m^2/s and 10 m^2/s at the boundary of an eddy. For a typical isolated structure of radius 50 km, a simple scaling law gives a duration of 8 years before complete decay. Thus, for an isolated eddy, the initial water mass trapped in the core can remain unchanged for long periods of time, except at the boundary. There, intrusions directly affects the properties of the trapped water and thus the tracer transport across the boundary.

Previous studies, mainly using satellite altimetry fields, have attempted to quantify eddy transport by using proxies to calculate eddy volumes. Eulerian and Lagrangian criteria have been used to obtain an overall estimate of the effect of eddies on tracer transport (Beron-Vera et al., 2013; Hunt et al., 1988; Okubo, 1970; Weiss, 1991b). Although the development of satellite altimetry has brought real progress in the monitoring of ocean eddies, it only provides access to smoothed (in time and space) sea surface heights. The surface geostrophic velocities are derived from the latter. However, they often do not correspond to the effective eddy core velocities (Bashmachnikov & Carton, 2012; Ienna et al., 2022; Subirade et al., 2023). This is partly due to the space-time resolution and smoothing applied to the satellite altimetry products, but also to the fact that eddies detected by satellite altimetry are not always surface intensified eddies (their core may be located well below the ocean surface and mixed layer). This suggests that satellite data, including satellite altimetry, may not be sufficient to represent the kinematic and dynamical properties of eddies, nor their 3D properties. Therefore, the large set of Eulerian and Lagrangian eddy estimates available from satellite data alone do not always adequately describe the characteristics and evolution of ocean eddies (e.g., Li et al., 2017; Sun et al., 2022).

To better understand the properties and behavior of eddies, we rely on *in-situ* observations collected during four oceanic cruises—EUREC4A-OA, Meteor 124, Meteor 160, and KB2017606—in the Atlantic Ocean, as well as on a theoretical framework. We propose to define the 3D boundary of mesoscale eddies using a new criterion based on the Ertel Potential Vorticity (EPV) (Ertel, 1942). The EPV is indeed a powerful tool for studying ocean dynamics. For a mesoscale eddy, it associates the existence of closed trajectories within which the EPV simply recirculates (in the absence of forcing and mixing) and the trapping of water masses (via isopycnal deflections). In the ocean, EPV mixing occurs at boundaries (ocean surface, bottom, and lateral boundaries, especially at shelf breaks, straits, and passages) (Benthuysen & Thomas, 2012; Welander, 1973); EPV mixing also occurs at the edges of eddies and within fronts. Previous studies of potential vorticity dynamics have quantified the effects of forcing and mixing processes on the EPV distribution (Marshall & Schott, 1999; Marshall & Speer, 2012). In the present study, we show how EPV can be used to define the 3D eddy boundary. In particular, we propose a new criterion that we compare with other previously published criteria as well as the Richardson number, which is well

known for studying symmetric instability and vertical mixing (Large et al., 1994; Pacanowski & Philander, 1981; Yu & Schopf, 1997; Zaron & Moum, 2009).

The paper is organized as follows. In Section 2, we describe the *in-situ* data we used to identify mesoscale eddies. We specify the resolution and measurement accuracy of the sampled anticyclonic eddies (AEs) and cyclonic eddies (CEs) in order to assess the relative errors of the derived quantities. In Section 3, we examine how eddy boundaries have been previously defined, and we focus on a subsurface eddy that is particularly well sampled by *in-situ* data to illustrate this comparison. In Section 4, we introduce the criterion we developed to define the eddy boundaries based on observations. In Section 5, we use a generic eddy to evaluate the magnitude of the criterion we define to support the observations. In Section 6, we reformulate the latter as a function of the Richardson number to relate it to criteria for symmetric instability. In Appendix A, we also propose a constraint on this criterion using a theoretical framework for semi-geostrophic baroclinic instability. This appendix details necessary conditions for instabilities using the Charney-Stern method (Kushner & Shepherd, 1995) at the eddy boundary and relates them to our criterion. In Section 7, we conclude the paper by summarizing our results.

2. Data and Methods

2.1. Collection of *In-Situ* Data

2.1.1. 2 AEs Sampled During EUREC^{4}A-OA Campaign

The EUREC^{4}A-OA campaign took place between the 20th of January and the 20th of February 2020 (Speich & Team, 2021; Stevens et al., 2021). We focus here on two AEs sampled along the continental slope of Guyana by the French RV L'Atalante. One of the anticyclones is a surface intensified eddy and has been identified as an NBC ring (Subirade et al., 2023). Its velocity field extends to a depth of −150 m. The other is a subsurface intensified anticyclone (with an intra-thermocline structure). Its core is located between −200 and −600 m depth. Hydrographic observations were carried out using Conductivity Temperature Pressure (CTD), underway CTD (uCTD), and Lower Acoustic Doppler Profiler (L-ADCP) measurements. A Moving Vessel Profiler (MVP) was also used to observe the surface-intensified eddy, but only for a few vertical profiles on the eastern side of the eddy (Speich & Team, 2021; L'Hégaret et al., 2022). A total of 25 and 24 CTD/uCTD profiles sampled the NBC ring and the subsurface eddy, respectively. The eddies velocity field was also measured by two ship-mounted ADCPs (S-ADCPs) with sampling frequencies of 75 and 38 kHz. Temperature and salinity were measured by the CTD with an accuracy of ±0.002°C and ±0.005 psμ, respectively. For the uCTD, the temperature and salinity accuracies are ±0.01°C and ±0.02 psμ, respectively. The S-ADCP measures horizontal velocities with an accuracy of ± 3 cm/s. See L'Hégaret et al. (2022) for more information on the *in-situ* data collected during the EUREC^{4}A-OA fieldwork.

The *in-situ* data were collected along sections, where stations or soundings provide vertical profiles at different distances from each other. We define the resolution of each section as the average of all distances between its successive soundings. For the particular section of the subsurface AE discussed here, the hydrographic data (considering only the CTD/uCTD profiles) have a horizontal (resp. vertical) resolution of 8.4 km (resp. 1m) and the velocity data have a horizontal (resp. vertical) resolution of 0.3 km (resp. 8m—we use the 38 kHz S-ADCP data). For the NBC ring, the data have a horizontal (resp. vertical) resolution of 10.3 km (resp. 1m) and the velocity data have a horizontal (resp. vertical) resolution of 0.3 km (resp. 8m—we use the 38 kHz S-ADCP data). In the following, either the resolution of the hydrographic data or that of the velocity data will be used, depending on the properties of interest.

2.1.2. 2 AEs and 1 CE Sampled During Meteor M124

The RV Meteor M124 cruise took place between 29th of February 2016 and 18th of March 2016 (Karstensen, Sabrina, et al., 2016) and crossed the South Atlantic ocean between Cape Town and Rio de Janeiro. We focus on two anticyclones (hereafter AEs) and one cyclone (CE) that appear to be Agulhas Rings and a Benguela Upwelling Eddy, respectively, sampled in the South Atlantic Ocean near the west coast of South Africa. Each eddy is associated with an extremum of the absolute dynamic topography derived from satellite altimetry (see Figure 1 of Karstensen, Sabrina, et al., 2016). These eddies extend vertically below −400 m depth. uCTD and S-ADCP measurements were performed to study their vertical structure. The 12, 11, and 8 uCTD profiles provide access to the thermohaline properties of the CE and AE, respectively. For each eddy, the hydrographic data have a

horizontal (resp. vertical) resolution of 21 km (resp. 1 m) and the velocity data have a horizontal (resp. vertical) resolution of 0.3 km (resp. 32 m).

2.1.3. 1 CE Sampled During Meteor M160

The RV Meteor M160 cruise took place between the 23rd of November 2019 and the 20th of December 2016 (Körtzinger & Team, 2021). We focus on a surface CE sampled along the east coast of Ilha do Fogo, Cabo Verde. For this eddy, interactions with the local topography may have affected its vertical structure. CTD, L-ADCP and S-ADCP measurements were used to investigate its vertical structure. 9 CTD profiles provide access to the thermohaline properties of this eddy. The hydrographic data have a horizontal (resp. vertical) resolution of 13.3 km (resp. 1 m) and the velocity data have a horizontal (resp. vertical) resolution of 0.3 km (resp. 8 m).

2.1.4. 1 AE Sampled During Kristine Bonnevie KB2017606

The RV Kristine Bonnevie cruise KB2017606 took place between the 10th of March 2017 and the 23rd of March 2017 (Bosse et al., 2019; Søiland & Team, 2017). We focus on a subsurface AE sampled in the open Arctic Ocean off the east coast of Norway. CTD and S-ADCP measurements were conducted to investigate its vertical structure. 20 CTD profiles provide access to the thermohaline properties of this eddy. The hydrographic data have a horizontal (resp. vertical) resolution of 5 km (resp. 1 m) and the velocity data have a horizontal (resp. vertical) resolution of 5 km (resp. 8 m).

For the purpose of our study, it is important that the *in-situ* section of the eddies crosses the eddy centers to avoid side effects. In Figure 1 we show, using the S-ADCP data and the eddy center detection method of Nencioli et al. (2008), that this was the case for the data we used. Also, we could only select eddies that were fully sampled to examine all their boundaries (upper, lower, and lateral). These conditions are rarely, if ever, met in the literature. As shown below, even eddies sampled during M124 fail this requirement.

2.2. Data Processing

For each campaign, the raw data were validated, calibrated, and then interpolated. Interpolation of vertical profiles sampled at different times had to be done carefully to avoid creating an artificial signal. To limit spurious effects, we only performed linear interpolations in $\vec{x}$ (here radial) and in $\vec{z}$ (vertical) directions. The data were then smoothed with a numerical low-pass filter of order 4 (scipy.signal.filt in Python). The choice of thresholds is subjective and depends on the scales studied. Here we consider mesoscale eddies, so we choose thresholds of the order of $L_x \approx 10$ km and $L_z \approx 10$ m for the horizontal and vertical length scales. Obviously, the cutoff period is chosen to be longer than the temporal sampling of the calibrated data. The grid size chosen for the interpolated data $(\Delta x, \Delta z)$ as well as the cutoff periods L_x and L_z are summarized in Table 1 for each cruise. Due to the coarse resolution of the M124 data, we expect the eddy boundaries for this cruise to be less defined.

Denoting $\left(\vec{x}, \vec{z}\right)$ the vertical plane of the section, and using smoothed data, the derivatives of a quantity a are approximated by a Taylor expansion of order one as follows:

$$\partial_x a(x + \Delta x,\, z) \approx \frac{a(x + \Delta x,\, z) - a(x,\, z)}{\Delta x} \tag{1}$$

$$\partial_z a(x,\, z + \Delta z) \approx \frac{a(x,\, z + \Delta z) - a(x,\, z)}{\Delta z} \tag{2}$$

Since the Taylor expansion has been truncated, the terms of order two $\frac{(\Delta x)^2}{2} \frac{\partial^2 a}{\partial x^2}$ have been neglected with respect to those of order one $\Delta x \frac{\partial a}{\partial x}$. An approximation of these second order term for the temperature, salinity, and velocity fields was calculated to substantiate this point. For instance, using data from the EUREC^{4}A-OA cruise, the second-order terms for temperature are, on average, about 1.10^{-6}°C/m horizontally and $0.6.10^{-4}$°C/m vertically. These values are small compared to the first order terms ($7.6.10^{-6}$°C/m horizontally and $2.5.10^{-2}$°C/m vertically). For temperature, second order terms thus represent 13% of first order terms horizontally and 0.03%

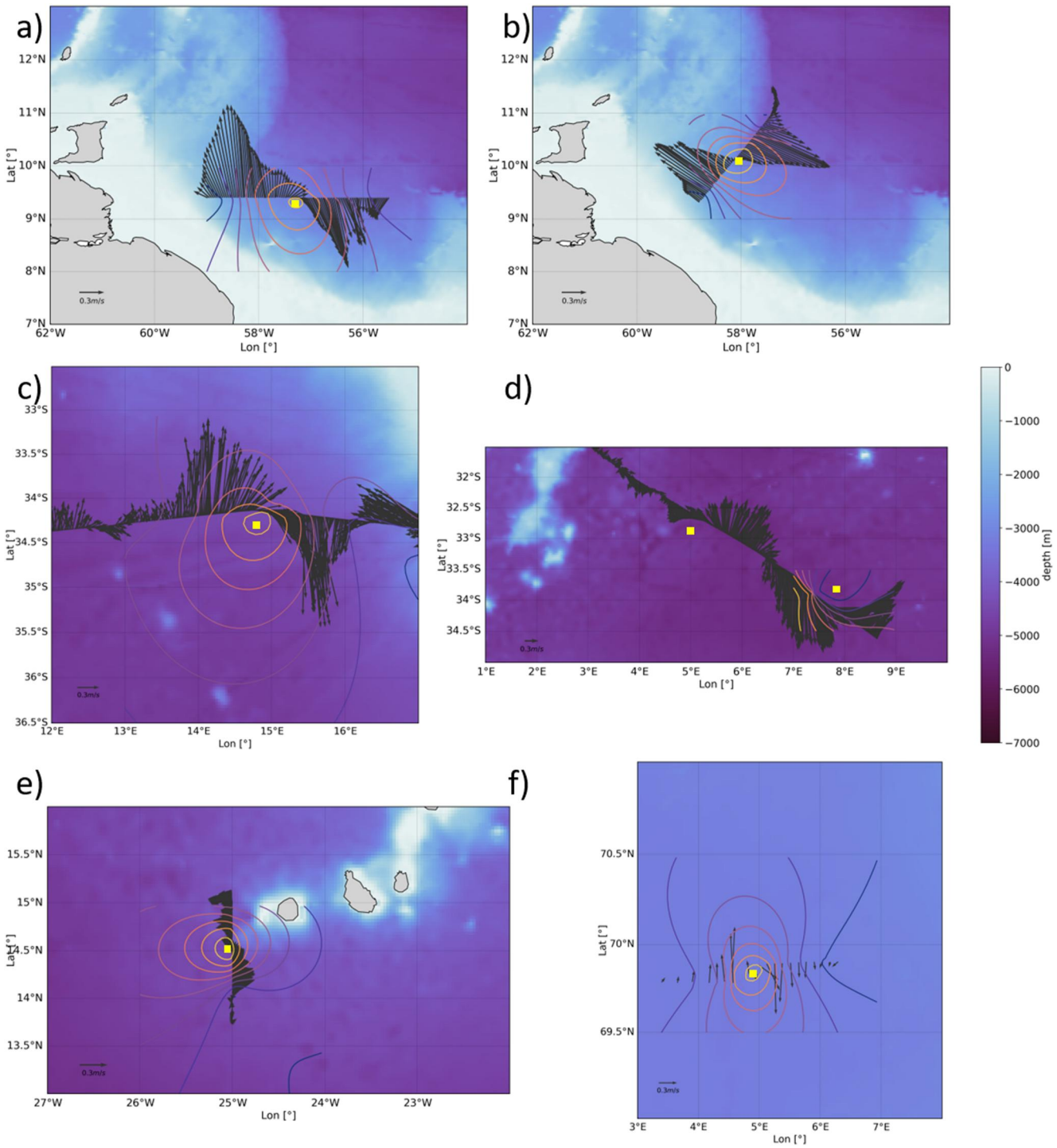

Figure 1. Velocity vector field at: −50 m for surface AE of EUREC^{4}A-OA (a), −300 m for subsurface AE of EUREC^{4}A-OA (b), −50 m for surface CE of M124 (c), −150 m for both AEs of M124 (d), −50 m for surface CE of M160 (e), −800 m for subsurface AE of KB2017606 (f). The regional bathymetry from the ETOPO2 dataset (Smith & Sandwell, 1997) is presented in the background as color shading as well as the estimated center (the yellow square) of the eddy computed from the observed velocities using Nencioli et al. (2008) method. The colored contours represent the loci of constant tangential velocity. The center is defined as the point where the average radial velocity is minimum.

vertically. For salinity and orthogonal velocity, the first-order horizontal (vertical) terms are larger than the second-order terms by factors of 10 (10^2) and 10^2 (10^3), respectively. With these approximations, the gradients of the different fields can be calculated reliably.

Table 1
Grid Size of Interpolated Data and Cutoff Periods for the Four Cruises

Cruise	Δx [km]	Δz [m]	L_x [km]	L_z [m]
EUREC^{4}A-OA	1	0.5	10	10
M124	1	1	25	40
M160	1	1	15	10
KB2017606	1	1	10	10

3. Eddy Boundaries Characterization From Previously Published Criteria

In the following, we describe several criteria which have been used to determine eddy boundaries from *in-situ* observations in previous studies. Uncertainties on the calculated quantities and basic information on mesoscale eddies are summarized in Table 2. For the sake of clarity, detailed criteria are illustrated only for the subsurface AE sampled during EUREC^{4}A-OA, where the vertical structure is very clear (see Figure 2). Vertical sections related to other mesoscale eddies can be retrieved in Supporting Information S1 (Figures S1 to S16).

3.1. Relative Vorticity

The first criterion we present is based on the relative vorticity ζ. The boundary of an eddy is defined as a closed contour where ζ changes sign, or more simply where $\zeta = 0$. This criterion has often been applied to altimetry maps using geostrophic velocity (Morvan et al., 2019; D'Addezio et al., 2019). It is a simple way to provide the upper boundary of a surface eddy or the lateral boundary of a subsurface eddy. It requires a knowledge of the horizontal velocity field but it does not require a reference profile.

To derive the relative vorticity (the vertical component of the vorticity vector), derivatives in two perpendicular horizontal directions are required. This is not possible with only one ship section. An approximation to the relative vorticity is the "Poor Man's Vorticity" (PMV) introduced by Halle and Pinkel (2003). They decompose the measured velocities into a transverse component $v_\perp$ (denoted V_o in Figure 3) and a longitudinal component $v_\parallel$. The relative vorticity is then approximated as $\zeta \approx 2\frac{\partial v_\perp}{\partial x}$. The factor of 2 allows the PMV to be equal to the actual ζ in a rotating solid vortex core. Rudnick (2001) and Shcherbina et al. (2013) used the derivative along the section of the perpendicular velocities without the factor 2. This factor depends only on the estimate of $\frac{\partial v\|}{\partial y}$. Here, we keep the latter approximation without further assumption:

$$\zeta \approx \frac{\partial v_\perp}{\partial x} \tag{3}$$

The errors on the relative vorticity can be calculated using finite differences. Using Equation 1, a local assessment of accuracy can be obtained:

$$\frac{\delta\zeta}{\zeta} \approx \frac{\delta V_o}{V_o} + \frac{\delta x}{l} \tag{4}$$

Table 2
Basic Properties of Mesoscale Eddies: Radius of Maximum Velocity R*[*km*], Maximum Isopycnal Deviation* H*[*m*], Maximum Velocity* V_m*[*m/s*], Rossby Number* $Ro = \frac{V_m}{f_0 R}$

Cruise	Type	R [km]	H [m]	V_m [m/s]	Ro	$\frac{\delta\zeta}{\zeta}$ [%]	$\frac{\delta EPV_z}{EPV_z}$ [%]	$\frac{\delta EPV_x}{EPV_x}$ [%]
EUREC^{4}A-OA	AE surf	121	70	1.14	0.44	2.9	3.6	17.0
EUREC^{4}A-OA	AE sub	71	220	0.96	0.66	3.5	3.8	18.6
M124	CE surf	67	120	1.53	0.28	2.4	2.8	59.7
M124	AE surf	58	200	1.27	0.26	2.9	3.1	58.0
M124	AE surf	55	105	0.95	0.28	3.7	4.2	75.5
M160	CE surf	49	50	0.46	0.09	20	22	36
KB2017606	AE sub	15	250	0.78	0.34	28.8	29.3	32.8

Note. Uncertainties of the relative vorticity $\frac{\delta\zeta}{\zeta}$[%], vertical EPV $\frac{\delta EPV_z}{EPV_z}$[%], horizontal EPV $\frac{\delta EPV_x}{EPV_x}$[%]. The uncertainties of the horizontal EPV are large. In fact, the calculation of this quantity combines two low resolution data sources: hydrographic data with low horizontal resolution and velocity data with low vertical resolution. Future oceanic cruises should take these relative errors into account in order to obtain measurements that are suitable for resolving the finer scales of the ocean.

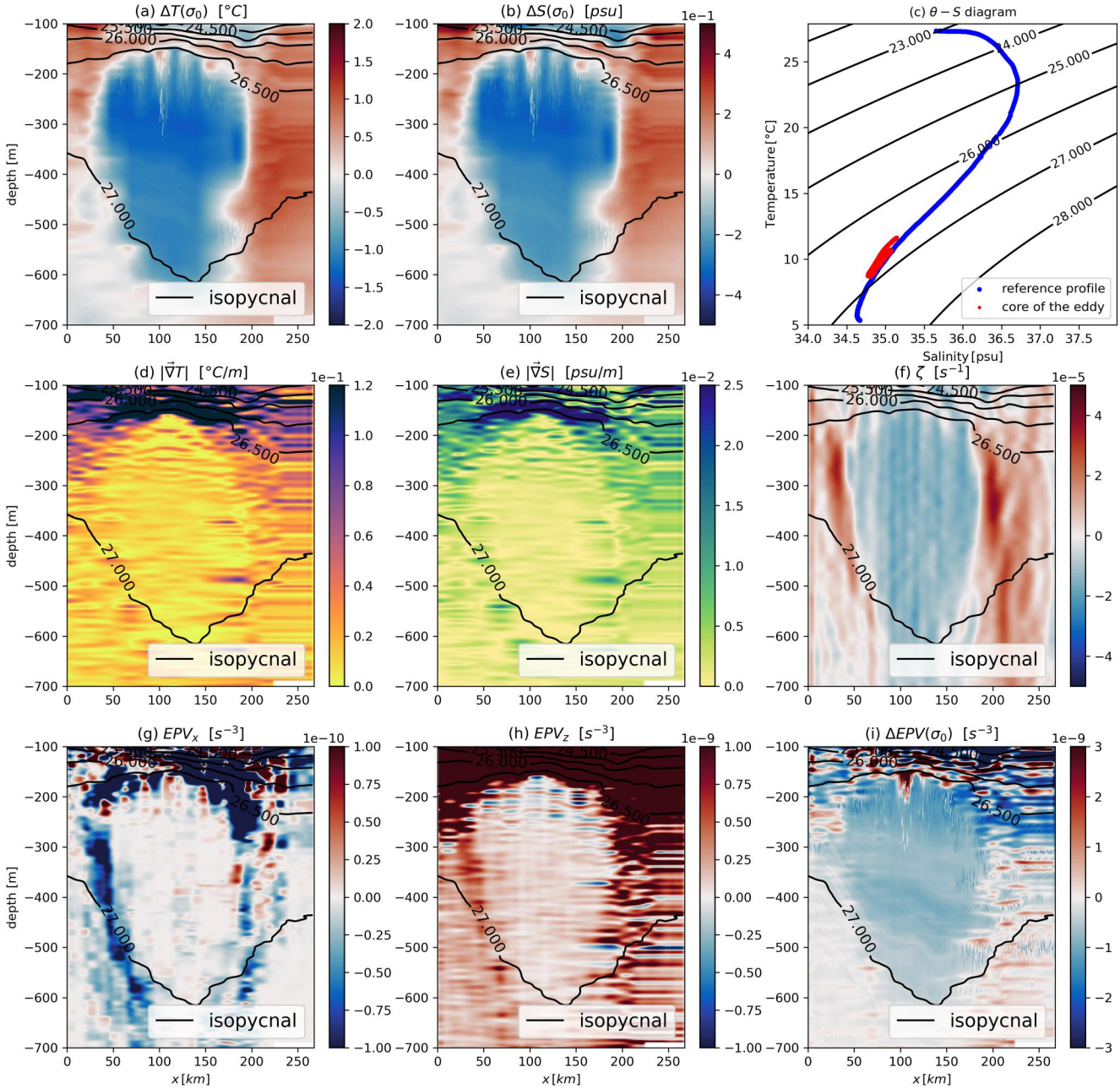

Figure 2. Vertical sections (x-axis = horizontal scale, z-axis = vertical scale) of different quantities: (a) thermal anomaly on isopycnal surfaces interpolated on geopotential levels; (b) salinity anomaly on isopycnal surfaces interpolated on geopotential levels; (c) $\theta - S$ diagram; (d) and (e) norm of 2D temperature/salinity gradients; (f) relative vorticity; (g) horizontal component of EPV; (h) vertical component of EPV; (i) EPV anomaly on isopycnal surfaces interpolated on geopotential levels. The thermohaline anomalies computed on isopycnals show a maximum at depth. For the $\theta - S$ plot, the reference profile in blue is the climatological mean computed using ARGO floats, and the red dots represent grid points for $x \in [100\text{ km}; 150\text{ km}]$ and $z \in [-400\text{ m}; -300\text{ m}]$. The data have been smoothed with a cutoff of 10 km horizontally and 10 m vertically. Isopycnals are shown as dark lines. The core is characterized by a homogeneous negative relative vorticity and EPV anomaly, and negative thermohaline anomalies.

where δx is the spacing between two measurement points (two stations) and l is a characteristic length scale taken here as the distance from the current point to the center of the eddy. Obviously, the smaller l and V_o, the larger the uncertainty, which can reach unlimited values. To avoid this pitfall and obtain an order of magnitude, we set $r = R$ the radius of the maximum velocity and $V(r) = V_m$ the maximum rotational speed of the eddy; the relative error in the relative vorticity is then given by

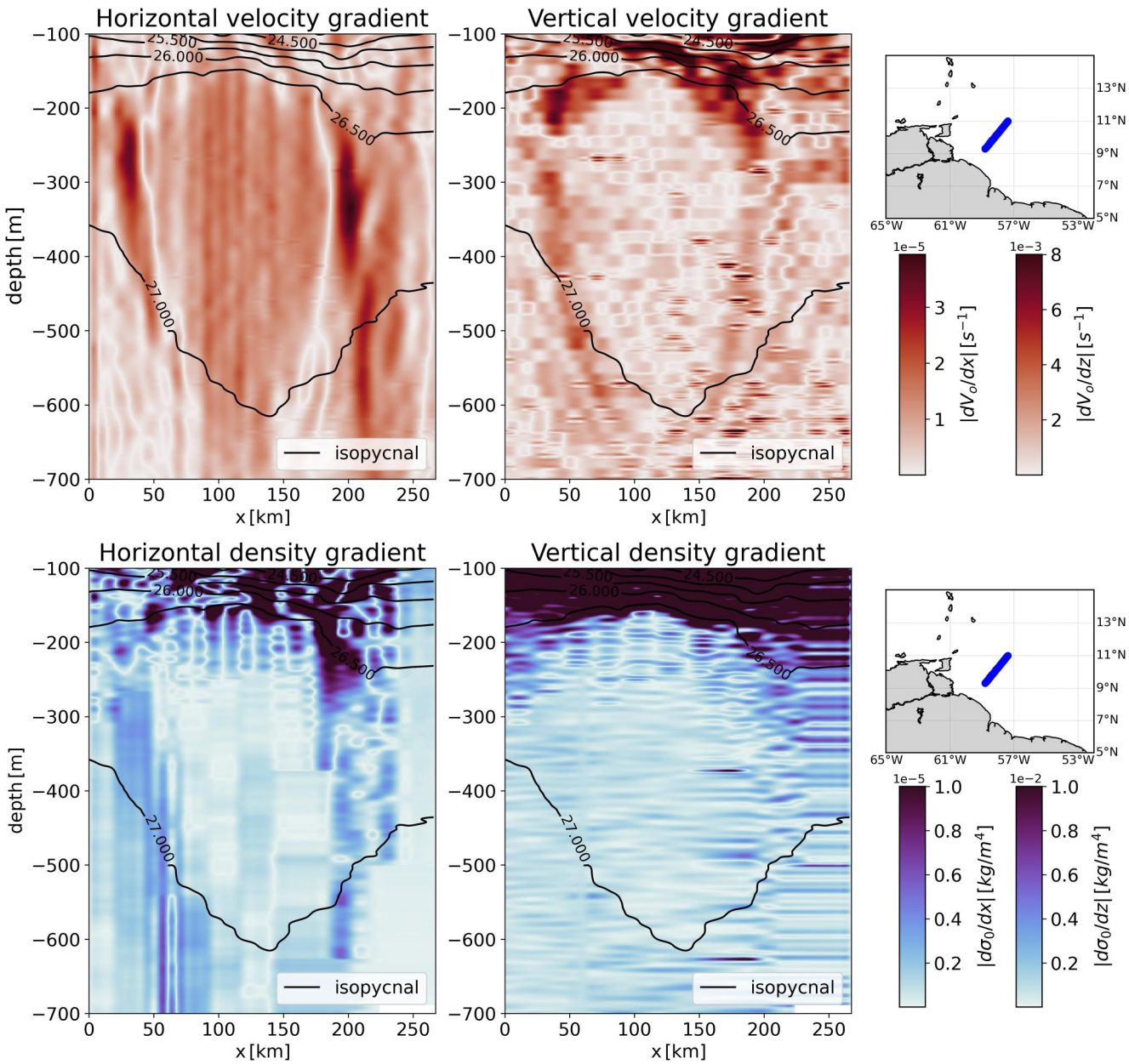

Figure 3. Vertical sections showing the modulus of the horizontal and vertical gradients for orthogonal velocity with respect to the ship's path V_o and the potential density field σ_0. At the boundary, the modulus of the vertical velocity gradient and the horizontal density gradient increase. On the contrary, the modulus of the horizontal velocity gradient and that of the vertical density gradient decrease. The small geographic maps show where the eddy was sampled.

$$\frac{\delta\zeta}{\zeta} = \frac{\delta V_o}{V_m} + \frac{\delta x}{R} \tag{5}$$

By taking into account the resolution of the S-ADCP data, uncertainties in the eddy relative vorticity can be calculated for all cruises.

However, this criterion has limitations. If the eddy is embedded in a parallel flow of uniform velocity U_0, a fluid particle can escape from the eddy core even if it is inside the $\zeta = 0$ contour (the relevant kinematic criterion then includes the ratio $V(r)/U_0$). Moreover, as shown in Figure 2f, the velocity field may tend to zero at the upper and lower boundaries of a subsurface eddy. Criteria based on surface vorticity are then ineffective in determining the eddy boundary.

More generally, it seems counterintuitive to have a locally defined border, since an eddy boundary has a finite horizontal extent; it is a region characterized by turbulence subject to external shear and instabilities (de Marez et al., 2020). From a Lagrangian point of view, a fluid particle located on the $\zeta/f_0 = 0$ line is in an unstable region and can be pulled into or out of the core. Finally, this criterion does not take into account the thermohaline properties of the water trapped in the core, although they do affect the global properties and dynamics of the eddy.

3.2. Thermohaline Anomalies on Isopycnals

When an eddy traps and transports a water mass, the temperature and salinity anomalies of the eddy core relative to the surrounding waters can help determine the eddy boundary. The eddy boundary is the region where the surrounding and trapped waters converge. Thus, a priori, temperature and salinity anomalies on isopycnic surfaces disappear there. Taking T^* and S^* as two reference temperature and salinity profiles (out of the eddies) and T and S as profiles (in the eddies), the thermohaline anomalies on isopycnic surfaces are defined by:

$$\forall\, \sigma_0, \quad \Delta T(\sigma_0) = T(\sigma_0) - T^*(\sigma_0) \tag{6}$$

$$\forall\, \sigma_0, \quad \Delta S(\sigma_0) = S(\sigma_0) - S^*(\sigma_0) \tag{7}$$

where σ_0 is the potential density with respect to the surface pressure. It is interesting to note that the compressibility of seawater is low for the studied eddies. Therefore, the T/S fields will be correlated and the anomalies will show similar structures.

The best choice of the reference profile has been the subject of several studies. Here we use the methodology developed by Laxenaire et al. (2019). A climatological average of temperature/salinity/potential density is computed over the geopotential levels, in a domain containing the sampled eddy. A square of side 0.5° is constructed around the estimated center of the eddy so that the center is at the intersection of the diagonals. Then all temperature, salinity, and potential density profiles sampled by Argo profiling floats over 20 years (Coriolis.eu.org) in this area are assembled and their values averaged over the geopotential levels.

In Figure 2 these anomalies are plotted (panels (a) and (b)) at the geopotential level. In fact, these anomalies are computed on isopycnal surfaces, but interpolated to geopotential levels to facilitate comparison with other criteria. The isopycnal anomalies (dark lines) are consistent with the anticyclonic nature of the eddy. Large negative temperature and salinity anomalies occur between −150 m and −600 m depth, showing that a heterogeneous water mass is trapped in the eddy core. The surrounding water is warmer and saltier than the core. Panel (c) showing the θ_S diagram confirms this. The anomalies appear fairly uniform in the core of the eddy and decrease near the eddy boundary. Closer inspection shows that they are slightly more intense in the upper part of the core (between −250 and −350 m depth) and that they decrease slowly with depth. Small-scale patterns of these anomalies are observed in the upper part of the core and will be discussed further in Section 4.2.

Using these quantities, the boundaries of the vortex can be drawn using a zero line for ΔT or ΔS (Figure 1). These lines are used to locally define the upper, lower, and lateral boundaries of the eddy. When thermohaline exchange occurs at the boundary of an eddy, this boundary is actually spread out rather than point-like. Furthermore, the zero lines are also sensitive to the reference profiles and will therefore vary with different choices of T^* and S^*.

It should be noted that at the eddy boundary, due to the isothermal/isohaline deviation, the gradients of T and S, defined as:

$$|\vec{\nabla}(T,S)| = \sqrt{(\partial_x(T,S))^2 + \left(\partial_z(T,S)\right)^2} \tag{8}$$

increase (see Figures 2d and 2e). Characterizing the eddy boundary in terms of temperature or salinity gradients has two advantages over T or S anomalies: first, the region of intense T or S gradients is not pointwise but relatively widespread; second, they do not depend on a reference value. These quantities are calculated at geopotential levels.

3.3. Ertel Potential Vorticity on Isopycnals

Ocean eddies are associated with a rotating flow field around an axis, with closed current lines and with thermohaline anomalies due to the water mass trapped in their cores. Ertel's Potential Vorticity (EPV) (Ertel, 1942), which takes into account all these properties, has therefore often been used to characterize the structure of eddies. The EPV is a Lagrangian invariant under several assumptions: inviscid flow, incompressible fluid, and potential body forces (Egger & Chaudhry, 2009). In the ocean, the EPV is rarely conserved due to atmospheric forcing and energy dissipation (Morel et al., 2019). For subsurface eddies, far from the seafloor, changes in EPV are moderate for most of their life cycle.

EPV is generally defined for 3D, non-hydrostatic flows with arbitrary density fluctuations. Here, we simplify this general definition for an application to 2D *in-situ* data. We also apply the Boussinesq approximation and the hydrostatic equilibrium. Under these hypotheses, the vertical acceleration vanishes and in the EPV definition the term $1/\sigma_0 \approx 1/\sigma_0^{(0)}$, where $\sigma_0^{(0)}$ is a reference value taken here as an average over each profile of the considered section. With our simplifications, EPV takes the following form:

$$EPV = EPV_x + EPV_z = \left(-\partial_z V_o \partial_x b\right) + (\partial_x V_o + f)\partial_z b \tag{9}$$

where $b = -g\frac{\sigma_0}{\sigma_0^{(0)}}$ is the buoyancy and V_o is the orthogonal component of the velocity on the horizontal axis of the section. Note that although Equation 7 gives only a 2D approximation to the true value of EPV, no approximation to the shape of the vortex (e.g., axisymmetry) has been used. We can also compute the relative error on the EPV, given by.

$$\frac{\delta EPV_x}{EPV_x} = \frac{\delta_H b}{b} + \frac{\delta_H x}{l} + \frac{\delta_V V_o}{V_o} + \frac{\delta_V z}{\delta z} \tag{10}$$

$$\frac{\delta EPV_z}{EPV_z} = \frac{\delta_H b}{b} + \frac{\delta_H z}{H} + \frac{\delta_V V_o}{V_o} + \frac{\delta_V x}{l} \tag{11}$$

where δ_H refers to the uncertainty in the hydrological data and δ_V to the uncertainty in the velocity data. To calculate the uncertainty in buoyancy, we use the linearized equation of state:

$$\delta_H b = \frac{-g}{\sigma_0^{(0)}}\delta_H \sigma_0 = \frac{-g}{\sigma_0^{(0)}}(-\alpha \delta_H T + \beta \delta_H S) \tag{12}$$

where g is gravity, α and β are averages over the section of the ship.

At the edge of the eddy, the isopycnals deviate sharply from the equilibrium depth of the environment, creating a horizontal buoyancy gradient. Thus, EPV_x is large, in contrast to the eddy core where EPV_x is small and EPV_z dominates. This suggests that EPV_x is a better criterion for eddy boundaries. Note that without a lateral buoyancy anomaly and without a baroclinic velocity term, EPV_x no longer exists.

Since eddies are stratification anomalies, characterization of the core of the eddy can be achieved using *Ertel Potential Vorticity Anomaly*. The EPV anomaly, ΔEPV, relative to the seafloor is also used to locate the eddy, compute its volume and characterize its intensity. The EPV of the ocean at rest (hereafter $\overline{EPV}$) is:

$$\overline{EPV} = f\frac{d\bar{b}}{dz} \tag{13}$$

where $\bar{b}$ is the buoyancy reference profile in the area of the eddy which has been computed as described in Section 3.2. The *Ertel Potential Vorticity anomaly* is then calculated on isopycnal surfaces (i.e., using density as the vertical coordinate) as follows:

$$\forall \sigma_0, \quad \Delta EPV(\sigma_0) = EPV(\sigma_0) - \overline{EPV}(\sigma_0) \tag{14}$$

More precisely.

$$\forall \sigma_0, \quad \Delta EPV(\sigma_0) = EPV_x(\sigma_0) + \Delta EPV_z(\sigma_0) \tag{15}$$

$$\forall \sigma_0, \quad \Delta EPV_z(\sigma_0) = EPV_z(\sigma_0) - \overline{EPV}(\sigma_0) \tag{16}$$

As with thermohaline anomalies, this quantity is computed on isopycnic surfaces and then represented on geopotential levels. As observed in Figure 2i, the boundary of an eddy can be defined by the outermost closed contour of ΔEPV. This quantity takes into account both thermohaline anomalies and the velocity field. As before, the upper, lower, and lateral boundaries of the eddy appear clearly. However, the boundary remains locally defined (i.e., for each eddy in its own environment) and is strongly dependent on the reference profile.

To conclude this section, there are many diagnostics to characterize the core of the eddy and thus calculate its volume (a given isotherm or isohaline, or the total EPV anomaly). However, all these criteria depend on an arbitrary reference and are very sensitive to its choice (in particular to compute the eddy volume). In the following section, we propose a criterion to characterize the boundary of an eddy with less arbitrariness. We could have discussed other criteria such as the Okubo-Weiss criterion (Okubo, 1970; Weiss, 1991a). However, the latter criterion is difficult to apply to vertical sections without additional assumptions (e.g., axisymmetry).

4. The α − Criterion for Vortex Boundary Determination

4.1. The α − Criterion for Vortex Boundary

In the core of the eddy, EPV_z strongly dominates EPV_x. At the boundary, this dominance becomes less pronounced due to three combined effects. First, the horizontal buoyancy gradient increases due to cyclo-geostrophic equilibrium; further out, the isopycnals return to the equilibrium depth for the surrounding waters. Second, two different water masses meet at the boundary, creating a frontal region that is usually characterized by a large horizontal buoyancy gradient. Third, the horizontal shear of the tangential velocity decreases. Peliz et al. (2014) have observed these variations in the amplitude of the EPV component from a numerical simulation. Here, for the first time, we use the EPV component amplitude to characterize the eddy boundary using *in-situ* data for a wide range of mesoscale eddies. An example of the EPV_x and EPV_z components is shown in Figures 2g and 2h for the subsurface AE sampled during EUREC^{4}A-OA. The core of the vortex is characterized by a homogeneous region of low EPV_z (EPV_z approximately 2×10^{-10} s^{-3}) surrounded by a zone where the EPV_x is close to -1×10^{-10} s^{-3}. Thus, the eddy boundary can be characterized as the region where the quantity $|EPV_x/EPV_z|$ reaches an extremum. To illustrate this point, the modulus of the horizontal and vertical gradients of the two quantities V_o (orthogonal velocity with respect to the ship's trajectory) and σ_0 (potential density) are shown in Figure 3 for the same mesoscale eddy.

In the modulus, the vertical velocity gradient and the horizontal density gradient increase at the eddy boundary, reaching values of the order of 10^{-3} s^{-1} and 10^{-6} kg/m^4, respectively. On the contrary, the horizontal velocity gradient (or ζ) as well as the vertical density gradient decrease near the eddy boundary. According to Equation 7 this is consistent with EPV_x and EPV_z variations at the eddy boundary. A similar conclusion can be drawn for a cyclonic eddy.

It is worth noting that, in this article, we propose a "mesoscale" characterization of eddy boundaries, and the data have been filtered accordingly to reduce the intensity of smaller scale processes. Indeed, a large number of high-resolution *in-situ* observations have shown that energetic submesoscale processes (including fronts, filaments, and vortices) co-occur with mesoscale eddies. These submesoscale processes can have very low and even negative EPV (Shi & Wang, 2020; Z. Zhang et al., 2021) and typically have extreme $|EPVx/EPVz|$ ratios. Therefore, they may blur the true boundary of mesoscale eddies in the submesoscale resolving data. Here, we consider a mesoscale point of view with processes having a horizontal characteristic length scale larger than 10 km. From a smaller scales viewpoint, submesoscale processes will indeed modify this boundary, but with less intensity. Moreover, these submesoscale processes which have not completely disappeared from the filtered data concur to the finding that the boundary is not pointwise (see Figure 4).

In addition to submesoscale processes, internal gravity waves (IGW) can also introduce in large noise into the calculated $|EPVx/EPVz|$ ratios. Since a shipboard transect across a mesoscale eddy typically takes more than a

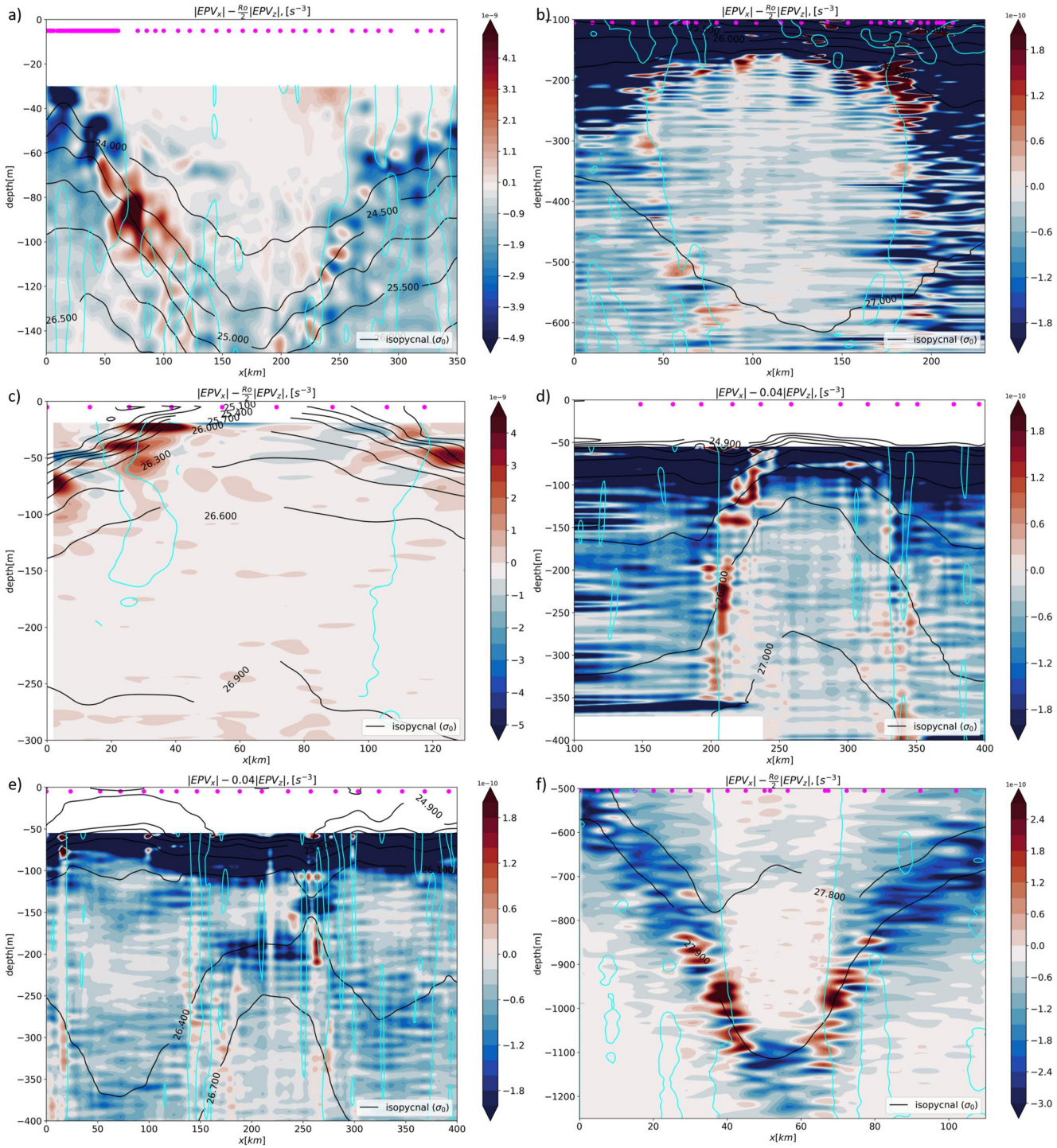

Figure 4. The $\alpha -$ criterion for different mesoscale eddies: (a) the surface AE observed during EUREC^{4}A-OA, (b) the subsurface AE measured during EUREC^{4}A-OA, (c) the surface CE sampled during M160, (d) the surface CE sampled during M124, (e) both surface AEs observed during M124, (f) the subsurface AE sampled during KB2017606. Magenta dots indicate the positions of the CTD/uCTD vertical profiles, cyan lines are locations where $\zeta = 0$ s^{-1} (due to data noise there is no unique extremum) and dark lines are isopycnals. The color bars have been chosen so that the red areas correspond to locations where $|EPV_x| - \alpha|EPV_z| > 0$, with α chosen as a fraction of the Rossby number. This criterion surrounds the core and extends from 10 to 50 km depending on the case and resolution. Note that this limit coincides with the inflection points of the isopycnals (see the theoretical part developed in the main text in Section 5).

day, the resulting eddy-resolving hydrographic data may also contain signals from IGW. Some recent papers have shown that IGW reduce the Kinetic Energy by about 25% on a global scale, for example, considering an entire ocean basin, and increase the forward energy cascade especially in regions of strong submesoscale fronts and filaments that dynamically deviate from the geostrophic equilibrium (Barkan et al., 2021). Other studies, such as Snyder et al. (2007), have shown that IGW mostly remain at the edge of eddies where submesoscale processes actually occur. Based on these arguments, from a mesoscale perspective and considering relatively short time scales, IGW will not significantly alter the mesoscale anomaly of stratification or velocity gradients.

Because *in-situ* data are sparse, the difference $|EPV_x| - \alpha|EPV_z|$ (where α is a scalar) is less noisy than the ratio $|EPV_x|/|EPV_z|$. In fact, due to noise, EPV_z may tend to zero at some spurious points, causing the ratio to diverge. We call the criterion α the characterization of the eddy core based on this condition:

$$|EPV_x| - \alpha|EPV_z| > 0 \tag{17}$$

This approach does not require a reference profile, which is its main advantage over other anomaly-based criteria. An application of this $\alpha -$ criterion is shown in Figure 4 for each eddy. It maps an area several kilometers wide, and the boundary is more irregular than for the pointwise criteria. From observations, the value $\alpha = \frac{Ro}{2}$, or even $\alpha = \frac{Ro}{3}$, seems to adequately characterize the 3D eddy boundaries. In each case, the lateral boundaries appear well marked, while the lower boundary is not well defined due to the weak velocity field at this location. The value of α depends on the resolution: a lower value was found for the coarse resolution of M124 compared to KB2017606 or EUREC^{4}A-OA, even if the three eddy Rossby numbers are close.

Consequently, the eddy boundary can be defined as a region whose length scale is comparable to the radius of deformation in one direction, but much smaller in the cross-direction; in the cross-direction, significant changes in buoyancy and velocity occur with substantially increasing gradients. In fact, this is the definition of a front given by Hoskins (1982) and confirmed by several studies (Archer et al., 2020; Katz, 1969; Voorhis & Hersey, 1964). At the frontal eddy boundary, water recirculates vertically during frontogenesis or when symmetric instability occurs. EPV_x and EPV_z are key terms in semi-geostrophic frontogenesis (Hoskins & Bretherton, 1972); they drive the dynamics of frontal regions. The associated vertical recirculation tends to flatten isopycnals. This has already been analyzed in numerical simulations (J. Chen et al., 2020). It has been shown that for high values of EPV_x, instabilities can occur that allow water masses to leak from the core of the eddy into the environment, where they are stirred and mixed. As a result, the baroclinic components of V_o and the horizontal gradient of σ_0 determine the amplitude of EPV_x with respect to EPV_z. Therefore, the value of α increases with the baroclinicity of mesoscale eddies.

4.2. $\alpha -$ Criterion Validation

In Figure 5 we focus only on the subsurface AE sampled during the EUREC^{4}A-OA field experiment. For this anticyclone, we apply and compare the previous eddy boundary criteria. First, we characterize the eddy core by the EPV anomaly on the outermost closed contour. This is $\Delta EPV < -5.10^{-10}\, s^{-3}$. We also plot the ratio $|EPV_x/EPV_z|$. The region of intense ratio (in dark red) agrees well with $\zeta = 0$ (dark green lines) around the core. It also agrees with the $\Delta T(\sigma_0) = 0$ and $\Delta S(\sigma_0) = 0$ contours both above the eddy and laterally. In fact, the thermohaline anomalies and the rotation of the eddy are related. Note that for other eddies, the boundary of the eddy core is best represented by non-zero values of these variables. This is a priori due to the choice of a reference profile that is not equal to a time average of the hydrology outside the eddies.

However, as shown in Figure 5, the lateral boundary is not a single line, but a relatively wide zone (sometimes reaching 30 km in width). In fact, lateral intrusion and mixing occur at the eddy boundary (Joyce, 1977, 1984). In addition, the criterion is less accurate near the base of the eddy because the eddy velocity decreases with depth. Here, the eddy boundary appears to be more diffuse and exchange of water masses with the surrounding water can take place (in particular by double diffusion). We recall that for a given translational velocity of the eddy, the velocity field decreases with depth; thus, the ability to trap water according to the (Flierl, 1981) criterion depends on depth. This is clearly illustrated by the anticyclone we are studying.

Finally, the upper part of the eddy near −200 m depth is well characterized by both the EPV anomaly and the $\alpha -$ criterion. The tropical thermocline (defined by a steep vertical density gradient) is clearly visible at the top of

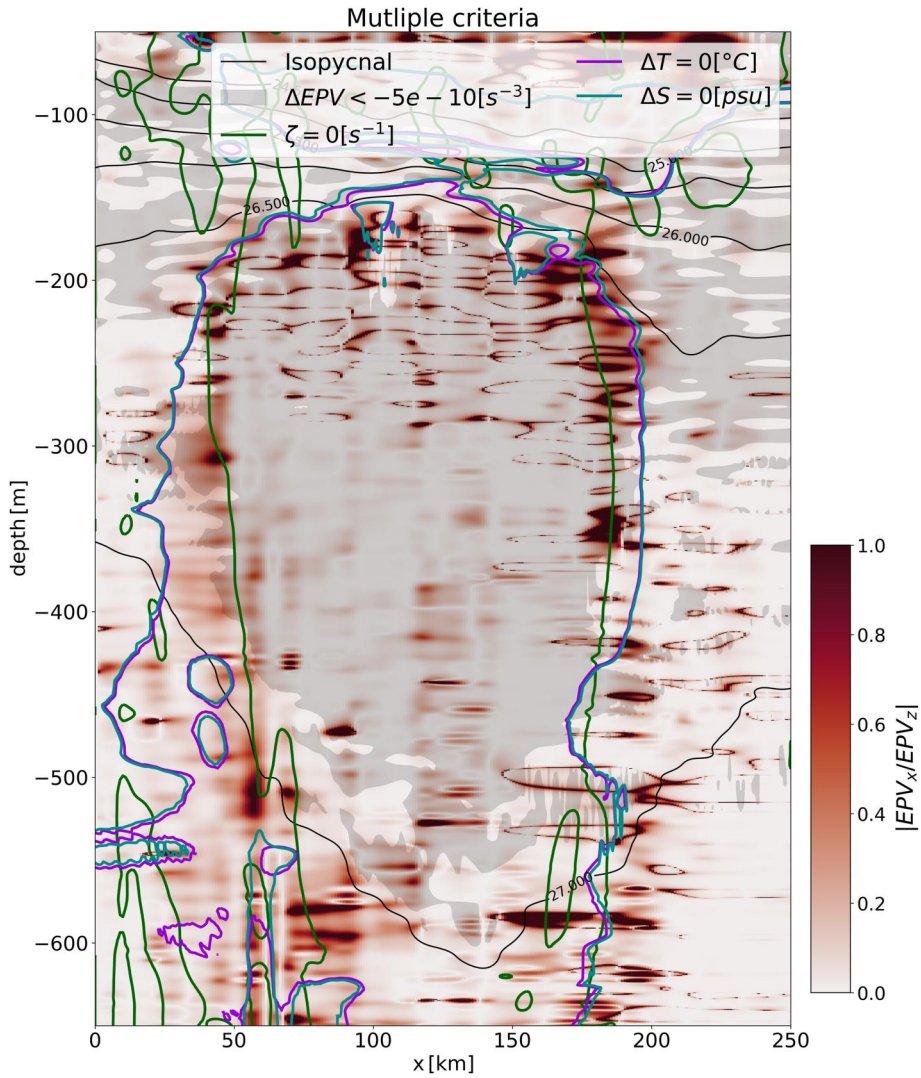

Figure 5. Vertical sections showing the comparison between the possible criteria for determining the eddy boundary. In the background, the dark red region corresponds to the α criterion, where the ratio EPV_x/EPV_z is plotted directly. The material boundary corresponding to $\Delta T = 0$ and $\Delta S = 0$ is plotted as purple and blue lines. The kinematic limit corresponding to a sign change of ζ is represented by a green line. Regions where $\Delta EPV < -5 \times 10^{-10}$ s^{-3} are plotted in light gray.

the eddy. Small-scale structures appear between −200 m and −300 m depth in the core of the eddy. They correspond to stair-like features in the temperature and salinity profiles (see Figure 6). Such features have been commonly observed in the northwestern tropical Atlantic by previous studies (Bulters, 2012; Fer et al., 2010). Staircases also occur at the top of the eddy core; they are detected by the $\alpha -$ criterion due to the strong vertical buoyancy gradient.

We now compare the $\alpha -$ criterion with the previously published Eulerian and Lagrangian criteria. First, many of these criteria are based on satellite altimetry data, which do not provide access to the 3D eddy structure. Second, our criterion can be applied to *in-situ* data, to numerical model results, or to sea surface height maps, allowing comparisons. Third, this criterion takes into account both the thermohaline anomaly and the rotating flow, which is not the case with all other criteria. Fourth, it provides a way to qualify and quantify the coherence of mesoscale eddies. In fact, the α value describes the intensity of eddy boundaries. The stronger the thermohaline anomalies, the more intense the α at the boundary. Determining the evolution of α gives access to the evolution of the 3D structure of an eddy and its coherence. Fifth, this criterion is complementary to the EPV anomaly criterion; in fact, it determines a boundary region where lateral water mass exchange takes place, rather than a single, well-located

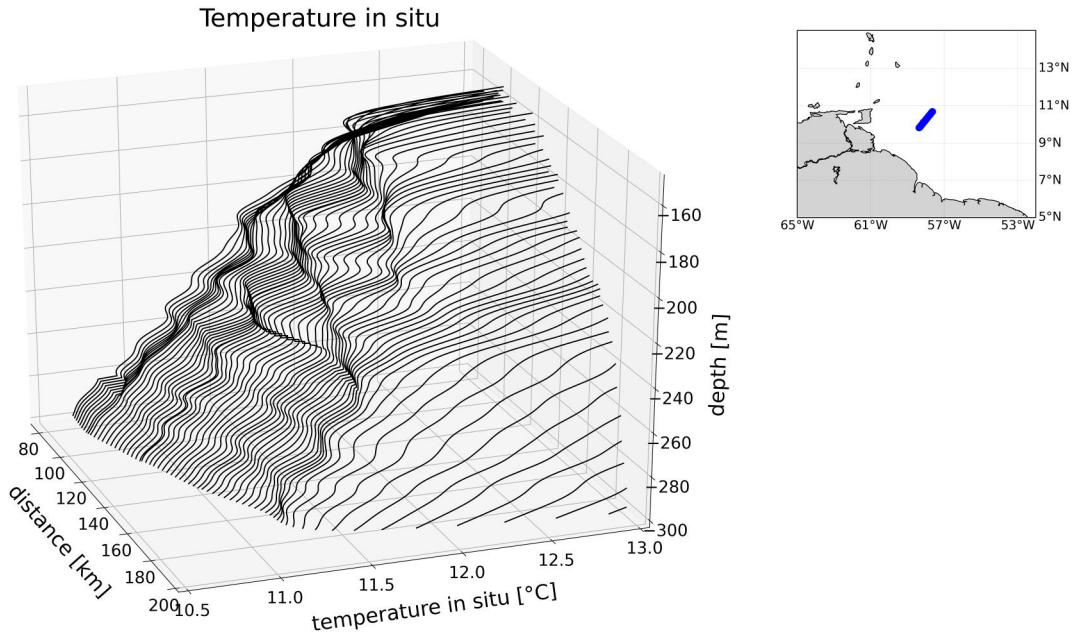

Figure 6. Staircases in the temperature profiles at the top of the subsurface eddy. The *x*-axis is the same horizontal scale as in Figure 1 but it starts at 80 km for more clarity. Each line is a vertical profile for temperature. Quick variations of these lines create a staircase shape (Bulters, 2012).

eddy boundary. Since the eddies are constantly responding to the background flow, the isopycnals adjust to this external forcing in the region where they develop. It should also be noted that this region is close to an inflection point of the isopycnal surfaces.

4.3. Modeling the Vortex Profile and Estimating the Influence of the Spatial Resolution

The $\alpha -$ criterion is sensitive to data resolution. To study the influence of the data resolution on the results, we have developed a simple model. This model is applied here to the EUREC^{4}A data, and more specifically to the AE of Figure 2. The data used in the model correspond to a vertical section with a resolution in $\vec{x}$ and $\vec{z}$ comparable to those obtained from oceanographic ships.

First, a generic model was fitted to the thermohaline anomalies on isopycnal surfaces. In the literature, Gaussian profiles have often been used to model thermohaline anomalies on these surfaces. In our study, a different function fits the data better (derived using the nonlinear least squares algorithm scipy.optimize.curve_fit in Python). We then calculated the density anomalies by applying the linearized seawater equation of state to use an explicit model equation. Next, we computed the geostrophic velocity by assuming that the eddy was in geostrophic and hydrostatic equilibrium. Actually, the maximum eddy Rossby number calculated using the maximum velocity estimated from the data was 0.61. However, for the purpose of this section, which is devoted to investigating the sensitivity of the results to the horizontal resolution of the data sampling, the geostrophic approximation is sufficient. Finally, we computed the ratio $|EPV_x/EPV_z|$ from the velocity field and the buoyancy anomaly.

This approach can be summarized in Figure 7.

- (1) - A nonlinear least squares algorithm has been used to fit an analytical expression to the data.
- (2) - The formula for the anomaly has been derived as follows:

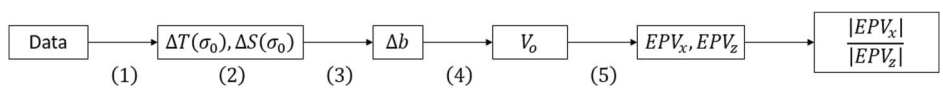

Figure 7. Steps followed: quantities computed at each step are written in boxes.

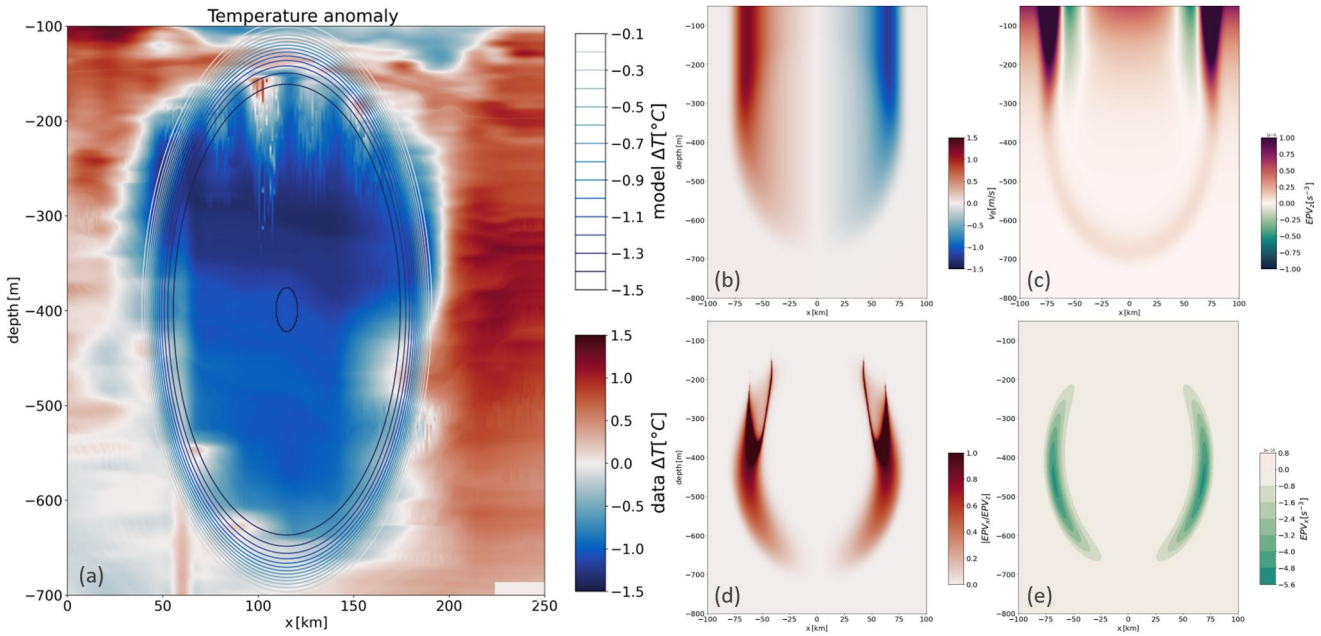

Figure 8. Vertical sections for the modeled anticyclonic eddy. (a) Comparison between data and model profile for the temperature anomaly, contours of constant value for the model are plotted. Fitting the gradient of the anomalies directly affects the EPV calculation and thus the α − boundary. (b) Azimuthal velocity for the model reaching a maximum at the sea surface. (c) Ratio $|EPV_x/EPV_z|$, (d) EPV_x, (e) EPV_z for the model.

$$\Delta a = A_0 \frac{\frac{10}{100\Gamma(0,1)}\exp\left(-\left(\frac{r}{71e3}\right)^{15}\right)}{\max\left(\frac{10}{100\Gamma(0,1)}\exp\left(-\left(\frac{r}{71e3}\right)^{15}\right)\right)}$$

with $r^2 = x^2 + (0.25z - 0.25 \times (-400))^2$ locating the center of the anomaly at ($x = 0$ m, $z = -400$ m). The factor 0.25 was chosen to account for the difference between the horizontal and vertical scales. This formula provides an elliptical pattern for the thermohaline anomaly on the vertical plane. The investigation of more complex functions approximating the anomaly are left for future studies. In the present work, we focused in the optimization by the nonlinear least squares algorithm only the radius 71 km, exponent 15, and center location at $z = -400$ m. It should be noted that a value of 15 for the exponent is very rare in the literature. This steepness can be explained when the external flow erodes the rotating flow. In this case, the eddy diffuses less momentum into the background flow (Legras & Dritschel, 1993; Mariotti et al., 1994).

- (3) - The linearized equation of state $\Delta\rho = \rho_0(-\alpha\Delta T + \beta\Delta S - \kappa\Delta P)$ was then used to obtain the density anomaly; α is the coefficient of thermal expansion, β is the coefficient of saline contraction, κ is the isentropic compressibility, ΔT and ΔS are the thermohaline anomalies on isopycnal surfaces, $\Delta p = p - p_{atmospheric} = -\rho_0 gz$ the hydrostatic pressure (we used $\rho_0 = 1026$ kg/m^3 as reference density for seawater). The reference values (ρ_0, T_0, S_0) have been calculated using the climatological average in the EUREC^{4}A region.
- (4) - The geostrophic balance $f_0\partial_z V_o = \partial_x \Delta b$ was then applied with a reference level (no flow condition) $V_o(x, z = -1{,}000\text{ m}) = 0$ m/s. The reference level has been chosen at −1,000 m in order to lie below the type of eddies we were focusing on (the NBC rings).
- (5) - Formula for EPV. We assume that the Boussinesq approximation and hydrostatic equilibrium hold. We use Equation 7.

The temperature anomaly calculated on the isopycnal surfaces is shown in Figure 8a as an example of step (2). The model does not fit the data perfectly. The geostrophic balance is not accurate near the tangential velocity peak, where cyclostrophic effects are not negligible. The eddy background is not modeled here, in particular the tropical thermocline, which causes the velocity field to decrease rapidly in the upper layers. The fields in the model are assumed to be stationary, which is not the case in reality. Finally, the f-plane approximation is used,

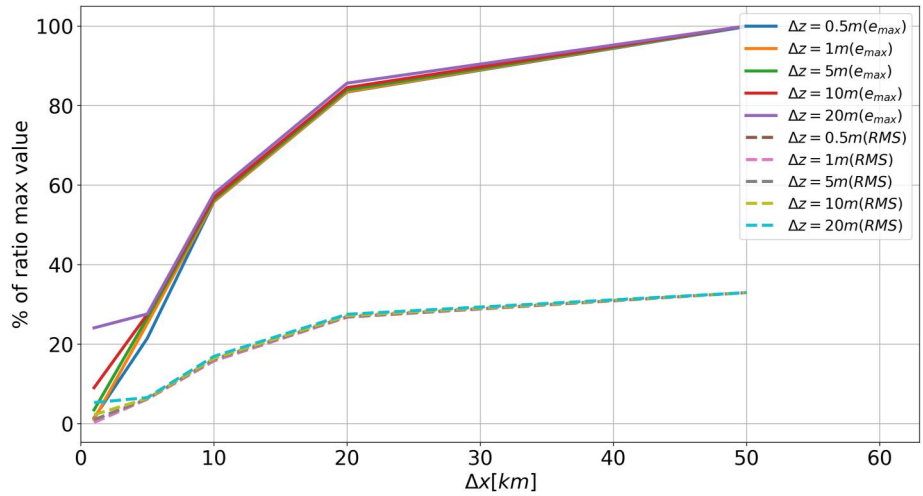

Figure 9. Maximal RMS and maximal error, in percentage of the ratio maximum value, as a function of horizontal resolution. Curves are plotted for various value of Δz.

whereas for large eddies the β-plane approximation would be more appropriate. For information, the steepness of the radial temperature (or salinity) profile can be explained by shear effects that may have stripped the outer layers of the eddy. Nevertheless, the quantities provided by the model (see panels (b), (c), (d) and (e)) seem to be in reasonable agreement with the data: V_o seems to be quite faithful, and EPV_x increases at the boundaries, as does the ratio $|EPV_x/EPV_z|$. The latter follows the region where the horizontal buoyancy gradient is large, which is the case in the observed AE. The shape of the eddy as well as the magnitudes of the anomalies are consistent with the observed eddy properties.

To evaluate the effect of spatial resolution on the $\alpha -$ criterion, we computed a very high resolution vertical section ($\Delta x = 100$ m, $\Delta z = 0.1$ m) as a reference. Other sections were then computed with lower spatial resolutions. As shown in Figure 8, the ratio $|EPV_x/EPV_z|$ diverges in the upper part of the eddy, near 300 m depth. This divergence is obviously not present in the observed eddy, which underlines the limitations of the model. Therefore, to calculate the difference between the high-resolution reference section and the lower-resolution sections, we consider only the lower part of the eddy at depths between 400 and 1,000 m.

With this assumption, the reference EPV ratio $Ra = |EPV_x/EPV_z|$ reaches its maximum of 1.342 at $z = -400$ m and $r = \pm 59$ km. The maximum error and the maximum RMS between a lower resolution profile and the reference profile are plotted to analyze the effect of resolution. The maximum error is defined as $e_{\max} = \max |Ra_{ref} - Ra|$, $r \in [-100; 100]$, $z \in [-1{,}000; -400]$. The results are shown in Figure 9.

This figure shows that the lower the resolution, the higher the error. The horizontal resolution mainly affects the accuracy of the results. The vertical resolution has less influence on the maximum error and the RMS. Even at the relatively high horizontal resolution (10 km) of the EUREC4A data, the maximum error is 0.8 or 58% of the maximum value of Ra. The resolution largely limits the accuracy of the results. However, the shape of the eddy boundary appears to be less sensitive to resolution. For example, at a horizontal resolution of 10 km, the RMS is 0.21 or 16% of the maximum Ra. In addition, *in-situ* data are often affected by noise, which is not considered here. In conclusion, resolution has a large effect on the quantitative values of the criteria, but a moderate effect on the shape of the eddy boundary.

4.4. An Experimental Range of α Values

In this section, the $\alpha -$ criterion is used to compare the intensity of the eddy boundaries and to obtain an experimental range of α values. Each boundary is characterized by the $\alpha -$ criterion as described above. The value of α indicates the intensity of the boundary. To quantify the intensity of the boundary, we numerically compute its area A_α in the $\left(\vec{x}, \vec{z}\right)$ plane. Obviously, the higher α, the smaller the area of the boundary: A_α is a decreasing function of α. α will reach higher values over a larger part of the total boundary area for a more intense eddy. In

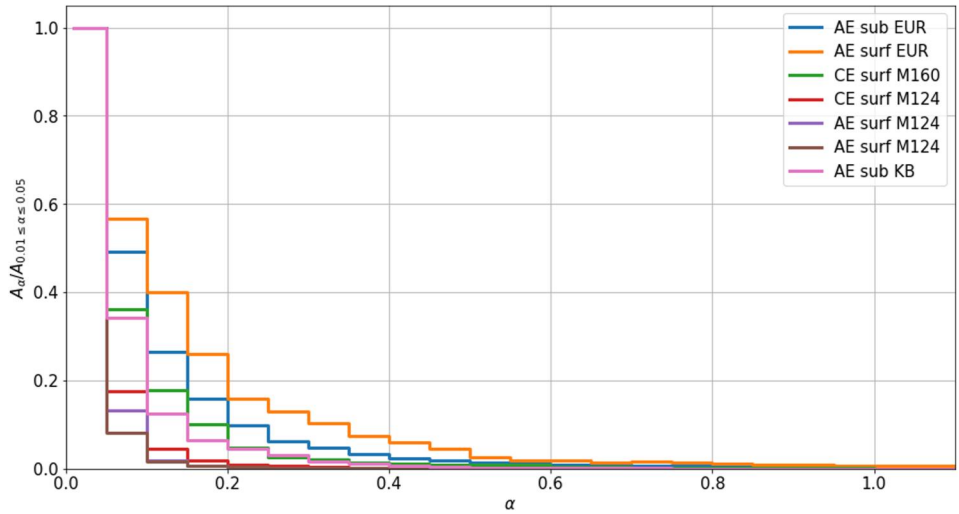

Figure 10. Eddy boundary intensity for the seven mesoscale eddies. For each bin $\alpha \in [0.05k; 0.05(k+1)]$ (except for the first step where $\alpha \in [0.01; 0.05]$), the area of the boundary where $0.05k \le |\frac{EPV_x}{EPV_z}| \le 0.05(k+1)$ is computed and arbitrarily normalized by $A_{0.01 \le \alpha \le 0.05}$. The ordinate axis represents the normalized limit. The abscissa axis shows the value of α.

this case A_α will decrease more slowly. What influences the intensity of the boundary is examined in the theoretical part. To compare the curves, A_α is arbitrarily normalized by $A_{0.01 \le \alpha \le 0.05}$, which is the area of the boundary when $\alpha \in [0.01; 0.05]$. For α varying from 0.01 to 1.1 with a bin of 0.05, A_α is plotted as a step function in Figure 10. As an example, the second step represents the area of the boundary for $\alpha \in [0.05; 0.01]$ normalized by $A_{0.01 \le \alpha \le 0.05}$. Note that the boundary region corresponds to a volume in space. Here, with 2D fields, only a portion of this volume can be observed.

In Figure 10 we observe that α is never greater than 1 for the studied eddies. Furthermore, 90% of the boundary region is characterized by $\alpha \le 0.4$. As before, the resolution seems to determine the value of α, as the three lower curves are those of the coarse M124 data.

To quantify the decay of an eddy boundary, it will be interesting to study the evolution of these curves with time. As an eddy boundary weakens due to interaction with the topography or in the presence of external shear flows, its boundary is eroded, and we therefore expect the quantity $\int^\alpha A(\alpha')/A_{0.01}\, d\alpha'$ to decrease.

4.5. A Subsequent Criterion: Comparison Between ΔEPV_z and EPV_x

Using the same idea, since EPV_x is stronger at the eddy boundary (Y. Zhang et al., 2014; Y. Chen et al., 2021), the ratio $|\Delta EPV_z/EPV_x|$ can be used to separate the eddy core from its boundary.

Figure 11 shows that $|\Delta EPV_z/EPV_x| > \beta$, with $\beta = 50$ in the core of the subsurface AE sampled during EUREC^{4}A-OA, decreases to a ratio of 5 or less at the edge of the eddy. The value of 50 was chosen to obtain the last closed contour of $|\Delta EPV_z/EPV_x|$ from the center of the eddy. Therefore, the EPV anomaly in the eddy cores is mainly due to the EPV_z term. Since the EPV anomaly is due to the anomaly in stratification and relative vorticity, the influence of the EPV_x term becomes significant only at the eddy boundary. This is in agreement with the results previously obtained for the $|EPV_x/EPV_z|$ ratio. To our knowledge, this calculation has never been performed on *in-situ* data. Previous studies have neglected the EPV_x term in the EPV anomaly (e.g., Paillet et al., 2002) because it only slightly modifies the wavy shape of the boundary. In fact, this term emphasizes and quantifies the frontality of the eddy boundary.

A drawback of this criterion is that it also detects regions where $\Delta EPV_z > EPV_x$ outside the core of the eddy. Therefore, one must assume the connectedness of the core to eliminate these outlying regions. Finally, note that the lower boundary of the eddy is more obvious with this criterion. According to the last closed contour, the base of this anticyclone is located near $z = -650$ m.

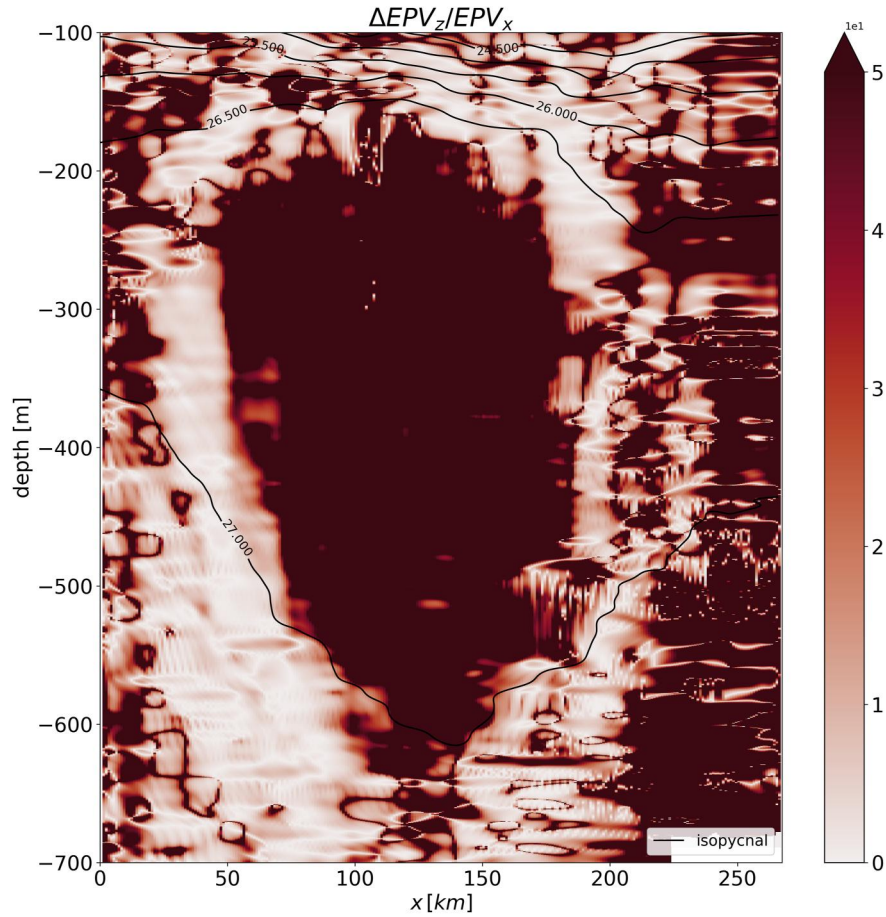

Figure 11. Vertical section showing the modulus of the ratio between ΔEPV_z and EPV_x; colors have been saturated to obtain a homogeneous core. The clear boundary represents the region where the baroclinic term EPV_x has a non-negligible value compared to ΔEPV_z.

5. Theoretical Aspects and Discussion

5.1. α − Criterion for a Generic Eddy

The purpose of this section is to apply the criterion to a generic eddy in an otherwise quiescent idealized ocean. Our goal is to illustrate the criterion and find orders of magnitude for the α values. Consider an isolated and stable circular eddy near the surface of a continuously stratified ocean. We assume the $f-$ plane approximation ($f = f_0$). Assume that this eddy traps water in its core, so that the density field ρ can be decomposed into cylindrical coordinates as follows:

$$\rho(r,z) = \overline{\rho}(z) + \rho'(r,z) \tag{18}$$

$$\overline{\rho}(z) = \rho_w + \rho_1 e^{z/D} \tag{19}$$

$$\rho'(r,z) = \rho_0 e^{z/H} e^{-r^\delta/R^\delta} \tag{20}$$

$\overline{\rho}(z)$ is the stratification of a quiescent ocean composed of ρ_w = 1,000 kg/m^3 the water density, ρ_1 the surface density anomaly relative to ρ_w, and D the vertical scale of the undisturbed stratification. The perturbed density profile adds an exponential power anomaly of amplitude ρ_0 and steepness δ so that for $\delta = 2$ we recover a Gaussian profile (Carton et al., 1989). The characteristic radius of the profile is noted as R. This anomaly decreases exponentially in the vertical direction on a scale H. Assuming that the eddy is in hydrostatic and

geostrophic equilibrium, the velocity field v_θ, the pressure anomaly p', and the density anomaly ρ' are related by the following equations.

$$f_0 v_\theta = \frac{1}{\rho_w}\frac{\partial p'}{\partial r} \tag{21}$$

$$\frac{\partial p'}{\partial z} = -g\rho' \tag{22}$$

As for the model, for simplicity, only the geostrophic component of the velocity is calculated, but as we have seen, the eddy Rossby number may not be small.

Substituting the expression ρ' into these equations and calculating the pressure and velocity leads to:

$$p'(r,z) = p_0 e^{z/H} e^{-r^\delta/R^\delta} \tag{23}$$

$$v_\theta(r,z) = V_0\left(\frac{r^{\delta-1}}{R^{\delta-1}}\right) e^{z/H} e^{-r^\delta/R^\delta} \tag{24}$$

with $p_0 = -\rho_0 g H$ and $V_0 = \frac{-\delta p_0}{f_0 \rho_w R}$. The relative vorticity can also be computed with the velocity field and we introduce the buoyancy field:

$$\zeta(r,z) = \frac{\delta V_m}{R}\left(\frac{r^{\delta-2}}{R^{\delta-2}}\right)\left(1 - \frac{r^\delta}{R^\delta}\right) e^{z/H} e^{-r^\delta/R^\delta} \tag{25}$$

$$b(r,z) = -g\frac{\rho}{\rho_w} \tag{26}$$

In order to find variations of α as well as an order of magnitude, each quantity is normalized. Therefore, we introduce the normalized variables $\overline{r} = r/R$ and $\overline{z} = z/H$, the normalized quantities $\overline{b} = b/g$, $\overline{v_\theta} = v_\theta/V_m$ and $\overline{\zeta} = \zeta/(\delta V_m/R)$, and the parameters $\xi = H/D$, $\gamma = \rho_1/\rho_0$. We then obtain:

$$\overline{b}(r,z) = -1 - \frac{\rho_0}{\rho_w}\left(\gamma e^{\xi\overline{z}} + e^{\overline{z}} e^{-\overline{r}^\delta}\right) \tag{27}$$

$$\overline{v_\theta}(r,z) = \overline{r}^{\delta-1} e^{\overline{z}} e^{-\overline{r}^\delta} \tag{28}$$

$$\overline{\zeta}(r,z) = \overline{r}^{\delta-2}\left(1 - \overline{r}^\delta\right) e^{\overline{z}} e^{-\overline{r}^\delta} \tag{29}$$

ξ represents the influence of the perturbed stratification relative to that of the quiescent ocean. γ introduces the influence of the amplitude of the density anomaly generated by the trapped water relative to the amplitude of the density of the quiescent ocean. For an axisymmetric eddy in the $f-$ plane, the Ertel potential vorticity is written as follows

$$q = q_r + q_z = -\frac{\partial v_\theta}{\partial z}\frac{\partial b}{\partial r} + \left(\zeta + f_0\right)\frac{\partial b}{\partial z} \tag{30}$$

We normalize these quantities by $gV_m/(HR)$ and compute the ratio $\mathbf{R} = q_r/q_z$ using the normalized quantities introduced earlier, so that.

$$\mathbf{R} = \frac{q_r}{q_z} = \frac{\overline{q_r}}{\overline{q_z}} \tag{31}$$

$$= \frac{-\delta^2 R_o \left(\bar{r}^{\delta-1} e^{\bar{z}} e^{-\bar{r}^\delta}\right)^2}{\left(\delta R_o \bar{r}^{\delta-2}\left(1-\bar{r}^\delta\right) e^{\bar{z}} e^{-\bar{r}^\delta} + 1\right)\left(\gamma\xi e^{\xi\bar{z}} + e^{\bar{z}} e^{-\bar{r}^\delta}\right)} \tag{32}$$

where $Ro = \frac{V_m}{f_0 R}$ is the Rossby number. Equation 32 is the complete analytical expression for the limit of this generic surface eddy described by the $\alpha -$ criterion. As $\bar{r}$ tends to 0, **R** also tends to 0; this is consistent with the results obtained with the EUREC^{4}A-OA observations. However, the most interesting parameter is the limit of the eddy, mathematically when $\bar{r}$ tends to 1. Note that the denominator is a strictly positive regular function and that **R** is defined for all $\bar{r}$ in **R** and for all $\bar{z} \in]-\infty; 0]$. In particular.

$$\mathbf{R}(\bar{r}=1,\bar{z}) = \frac{-\delta^2 Ro}{F_{\xi,\gamma}(\bar{z})} \tag{33}$$

$$F_{\xi,\gamma}(\bar{z}) = \gamma\xi e^{\bar{z}(\xi-2)-2} + e^{1-\bar{z}} \tag{34}$$

As before, the denominator $F_{\xi,\gamma}$ is strictly positive, regular, and diverges when $\bar{z}$ tends to $-\infty$. As mentioned above, **R** is negative. Note that the boundaries of the eddy depend on the square of the slope of the velocity field, the Rossby number, the size of the buoyancy anomaly, and the ratio of the two characteristic length scales of the stratification (at rest and perturbed). The larger ρ_0 is compared to ρ_1, the larger **R** will be. And the further apart the isopycnals are, the smaller H is with respect to D and the larger **R** will be. This dependence is interesting because these terms are related to the baroclinicity of the eddy (related to the slope of the eddy velocity and the deviation from the background stratification due to the presence of the eddy) and to the nonlinearity of the velocity field. These properties determine the strength of the eddy boundaries (in terms of permeability for water exchange and dissipation) and thus control the cohesiveness or coherence of the eddy.

Taking into account the regularity of the denominator, **R** is bounded and:

$$|\mathbf{R}(\bar{r}=1,\bar{z})| \leq \frac{\delta^2 Ro}{\min_{]-\infty;0]} F_{\xi,\gamma}(\bar{z})} \tag{35}$$

A more thorough study of the denominator shows that for $\xi \leq 2$, its derivative with respect to $\bar{z}$ is negative and consequently $F_{\xi,\gamma}$ decreases at $]-\infty; 0]$ to reach its minimum at $\bar{z} = 0$, that is, at the surface. In this case the upper limit given by Equation 35 is $\frac{\delta^2 Ro}{\gamma\xi e^{-2}+e}$. The influence of the density anomaly parameters is clearly visible in this expression. For $\xi > 2$, $F_{\xi,\gamma}$ decreases at $]-\infty; \bar{z}_0]$ to reach a minimum at $\bar{z}_0 = \frac{3-\ln\gamma\xi(\xi-2)}{\xi-1}$. We can show that this quantity is always negative regardless of the value of γ.

In the literature, ξ depends on the ocean basin and the type of eddy, but an order of magnitude between 1.5 and 3 is given. In the case where $\xi = 3$, two isopycnals that were initially 50 m apart are now 150 m apart in the perturbed stratification. In parallel, ρ_0 and ρ_1 also depend on the eddy type and the ocean basin. As an application, for the subsurface AE sampled during the EUREC^{4}A-OA eddy studied in parts 4.2 and 4.3, ρ_1 is 26 kg/m^3 while ρ_0 is 0.1 kg/m^3 (see Figure 2 panel (c)), which means that γ is 260. Taking $\delta = 15$ (see the model in Section 4.3), $\gamma = 260$, $\xi = 2$, and $Ro = 0.6$, we get $\mathbf{R}(\bar{r}=1,\bar{z}) \leq 1.9$. This value is consistent with Figure 10, where almost 100% of the surface is characterized by a value of α less than 1.

5.2. Curvature of Isopycnals

In this section we provide a geometric interpretation of the $\alpha -$ criterion. In Figure 4, the boundaries of the vortices appear to coincide vertically with the inflection points of the isopycnals. Using theoretical considerations, we try to find out when this coincidence is verified.

Consider an isopycnal surface that is vertically displaced by the presence of an oceanic eddy in the $f-$ plane. On this isopycnal surface, the variations of the b-field are zero:

$$db = \frac{\partial b}{\partial r}dr + \frac{\partial b}{\partial z}dz = 0 \tag{36}$$

Let us note z_b the geopotential level of this isopycnal of value b. By definition, its variation with respect to r depends on horizontal and vertical gradients such that:

$$\frac{dz_b}{dr} = \frac{-\partial b/\partial r}{\partial b/\partial z} \tag{37}$$

Searching for an inflexion point leads to the following condition:

$$\frac{d^2 z_b}{dr^2} = \frac{1}{\partial b/\partial z}\left(-\frac{\partial^2 b}{\partial r^2} + \frac{\partial b}{\partial r}\frac{\partial^2 b/\partial z^2}{\partial b/\partial z}\right) = 0 \tag{38}$$

which can be re-written:

$$\frac{\partial^2 b}{\partial r^2}\frac{\partial b}{\partial z} = \frac{\partial^2 b}{\partial r \partial z}\frac{\partial b}{\partial r} \tag{39}$$

Assuming that the eddy is in geostrophic equilibrium, the radial buoyancy gradient can be expressed as a function of the velocity gradient using the thermal wind equation.

$$\frac{\partial^2 b}{\partial r^2} = f_0 \frac{\partial^2 v_\theta}{\partial r \partial z} \tag{40}$$

$$\frac{\partial^2 b}{\partial r \partial z} = f_0 \frac{\partial^2 v_\theta}{\partial z^2} \tag{41}$$

Re-injecting those expressions in Equation 39 leads to:

$$\frac{\partial^2 v_\theta}{\partial r \partial z}\frac{\partial b}{\partial z} = \frac{\partial^2 v_\theta}{\partial z^2}\frac{\partial b}{\partial r} \tag{42}$$

This reflects the link between the buoyancy field and the velocity field at an inflection point.

Now, we can apply the $\alpha -$ criterion. On the $\alpha -$ boundary of the eddy, we have:

$$|q_r| - \alpha|q_z| \geq 0 \tag{43}$$

which can be simplified because $\zeta \approx 0$ at the boundary. Developing Equation 43, the buoyancy and velocity fields are thus linked by:

$$\left|\frac{\partial v_\theta}{\partial z}\frac{\partial b}{\partial r}\right| \geq \left|\alpha f_0 \frac{\partial b}{\partial z}\right| \tag{44}$$

Then, we can compute the ratio between Equations 42 and 44, which leads to:

$$\left|\frac{\partial^2 v_\theta/\partial z^2}{\partial v_\theta/\partial z}\right| \leq \left|\frac{\partial^2 v_\theta/\partial r \partial z}{\alpha f_0}\right| \tag{45}$$

As in the previous section, we introduce the scales associated with each quantity: H for z, V_m for v_θ, and R for r. In order of magnitude, the isopycnal curvature corresponds to $\alpha -$ criterion in regions where

$$\alpha \leq Ro \tag{46}$$

where Ro is the Rossby number. We find the result of the previous section when it was shown that the ratio $\mathbf{R}$ is a linear function of Ro. This result is also consistent with Figures 4 and 10, when we found values of α close to the Rossby numbers of studied mesoscale eddies. For example, for the subsurface AE sampled during EUREC^{4}A-OA of Figures 2, figure 10 (blue curve) showed that 98% of the boundary zone was characterized by a α lower than 0.6, consistent with a maximum Rossby number of 0.61.

5.3. Relation to the Richardson Number

To complement this theoretical approach, we establish the relationship between α and the Richardson number, more precisely the locally defined gradient Richardson number. The gradient Richardson number Ri, often used to describe the stability of stratified shear flow (Monin & Yaglom, 1971), is defined as the ratio of the buoyancy frequency N^2 squared to the vertical shear squared, such that:

$$Ri = \frac{N^2}{\left(\partial_z v_\theta\right)^2} \tag{47}$$

where $N^2 = \partial_z b$ with the previous notation and $\partial_z v_\theta$ is the vertical shear for an axisymmetric and isolated vortex. It quantifies the relative importance of stratification on velocity shear. Vertical turbulent mixing has been observed to be greatly enhanced in regions of low (<1) Richardson number both in the laboratory (Thorpe, 2005; Turner, 1973) and in the ocean (Peters et al., 1988; Toole & Schmitt, 1987). This number is also involved in the symmetric instability (Buckingham et al., 2021; Thomas et al., 2013) and can be related to the theoretical elements above. For an axisymmetric vortex under geostrophic equilibrium, EPV can be rewritten so that:

$$q = -\frac{1}{f_0}\left(\frac{\partial b}{\partial r}\right)^2 + \left(\zeta + f_0\right) N^2 \tag{48}$$

As a result, after some computation, the gradient Richardson number Ri can be written as a function of α such that:

$$Ri = \frac{1}{\alpha(Ro_d + 1)} \tag{49}$$

with $Ro_d = \frac{\zeta}{f_0}$ the dynamical Rossby number (Stegner & Dritschel, 2000). According to Hoskins (1974), a necessary condition for symmetric instability is:

$$Ri < \frac{f_0}{\zeta + f_0} = \frac{1}{Ro_d + 1} \tag{50}$$

which is equivalent to,

$$Ri(Ro_d + 1) < 1 \tag{51}$$

and finally,

$$\alpha > 1 \tag{52}$$

which gives an upper bound for α values in order the boundary be stable.

Figure 12 contrasts the Richardson number with the $\alpha -$ criterion. For *in-situ* data, the vertical shear is approximated by $\partial_z V_o$, where V_o is the velocity orthogonal to the ship track. For cruises with horizontal resolution less than 10 km, the minimum of the Richardson number coincides with regions where α is large, consistent with theory. Although data noise creates artificial color patches, eddy boundaries are also characterized by $Ri < 1$, which are known to be regions subject to symmetric instabilities.

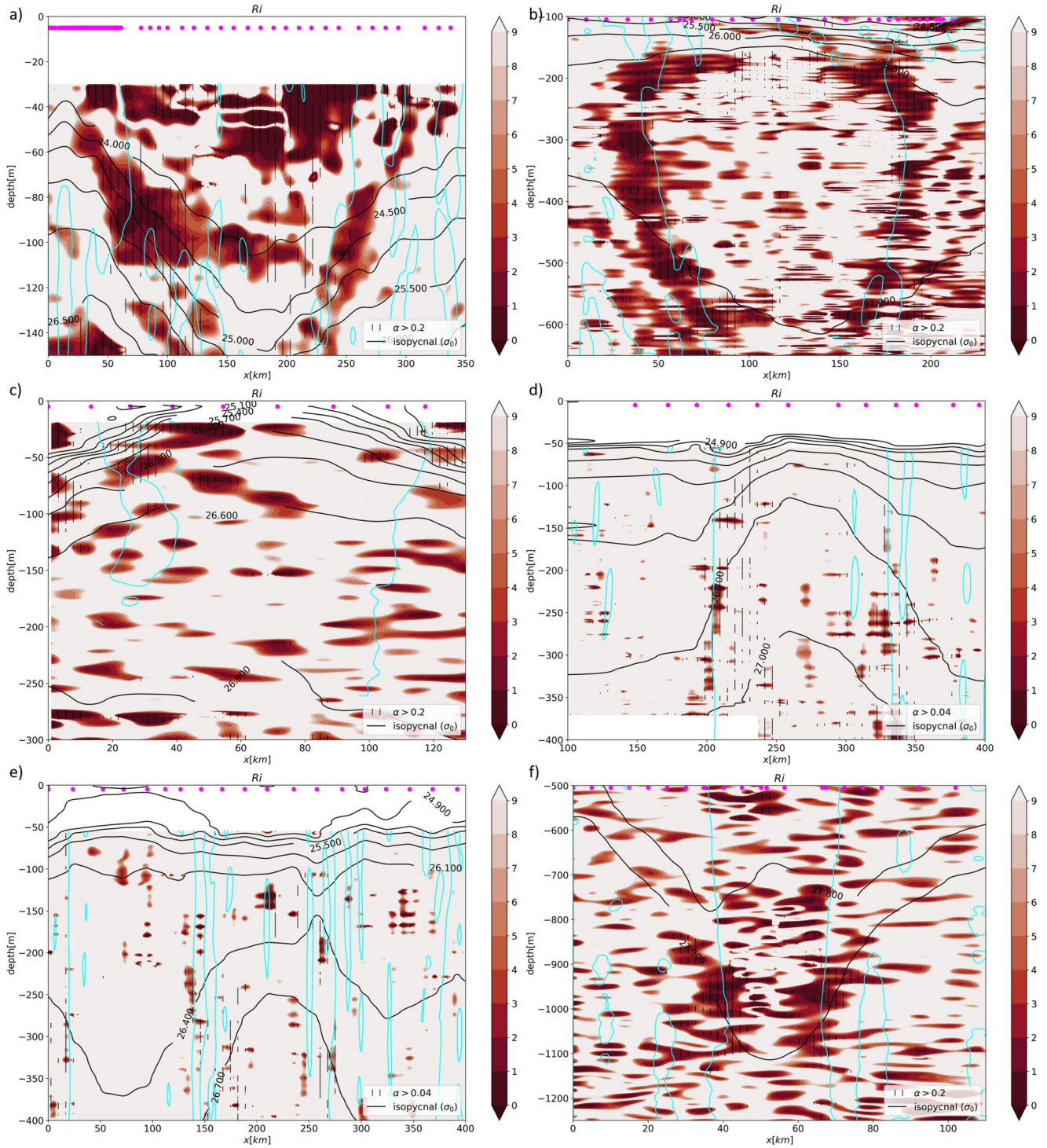

Figure 12. Relationship between Richardson number and α: (a) Surface AE of EUREC^{4}A-OA, (b) Subsurface AE of EUREC^{4}A-OA, (c) Surface CE of M160, (d) Surface CE of M124, (e) Both surface AEs of M124, (f) Subsurface AE of KB2017606. Magenta dots indicate locations of CTD/uCTD vertical profiles, cyan lines are locations where $\zeta = 0\ s^{-1}$ (due to data noise there is no unique extremum) and dark lines are isopycnals. Vertical hatching indicates regions where α is greater than a fraction of the Rossby number. Note that the coarse resolution of the M124 data was not sufficient to obtain a faithful Richardson number.

6. Conclusion

To gain insight into the nature of oceanic mesoscale eddies, whose dynamical properties, evolution and "coherence" are not yet well understood, we study a set of relatively high-resolution observations of seven

mesoscale eddies collected during four field experiments (EUREC4A-OA, M124, M160, and KB2017606). While mesoscale eddies have been previously studied from satellite observations, numerical simulations and idealized geophysical fluid dynamics frameworks or sparse *in-situ* profiles, these have limitations in correctly reproducing mesoscale processes. Based on analyses of this unprecedented set of observations, our study provides a detailed characterization of the core and boundaries of the observed eddies. We show that these structures are well defined in their properties and are best characterized by the Ertel potential vorticity framework.

In this work, we have focused in particular on the eddy boundaries, which are key to the existence and coherence of the eddies, since their strength and permeability control how they evolve and persist. Published studies have used different criteria to characterize these eddy boundary regions. However, they either found boundaries that were too narrow or relied heavily on a priori reference values. In this study, we propose a new criterion to characterize them, including their upper and lower bounds. This criterion compares the vertical and horizontal components of the Ertel potential vorticity. The eddy boundary is characterized by a relatively intense horizontal component of the EPV. When applied, the threshold on this component identifies a relatively broad region rather than a point boundary. The finite width of this region indicates that local turbulent processes are at work, allowing water mass exchanges and mixing between the eddy boundaries and the background. The boundary or frontal zone of the eddy is also characterized by steep isopycnal slopes and a baroclinic velocity field, upon which the intensity of the criterion (and hence the boundary) depends.

We show that the relative intensity of the horizontal component to the vertical component of the EPV depends on the slope of the velocity field, the Rossby number, and the vertical stratification anomaly, using a theoretical framework for a generic AE. This criterion ("relative intensity equal to the α threshold") coincides with the inflection points of the isopycnal surfaces when α is of order Ro. These results suggest that the strength of the eddy boundaries, and thus the ability of the eddy to remain coherent and not dissipate, is governed by the baroclinicity of the eddy, the degree of ageostrophy, and the intensity of the thermohaline anomaly over the background vertical stratification. This criterion can also be expressed as a function of the well-known Richardson number, which helped us to define a critical value of α for which instabilities can grow. To assess the robustness and generality of these results, this needs to be explored in more detail in future work.

This study also highlights the critical importance of not only vertical, but also horizontal high-resolution spatial sampling of thermohaline and velocity eddy properties. This is necessary for the minimization of errors in the criterion estimation as well as in the identification of eddy boundaries. Therefore, we recommend that future ocean observations should include adequate sampling spacing between vertical profiles. This recommendation also applies to the spatial resolution of numerical models.

Finally, future work should analyze other mesoscale ocean eddies that are well resolved in terms of observations and numerical simulations to verify the generality of the α criterion we have defined. Comparisons with Eulerian and Lagrangian criteria are also necessary for a better understanding and characterization of eddy coherence and the various processes that control it.

Appendix A: The Semi-Geostrophic Charney-Stern Criterion and a Restriction of α Values

The intensity of an eddy boundary depends on the Rossby number, the steepness of the velocity field, and the buoyancy anomaly as shown previously. Therefore, α is usually less than one. However, one may wonder if an upper bound on the α values can be found. In this section, we use the semi-geostrophic Charney-Stern criterion for vortex instability with a focus on the eddy boundary to find an upper bound on α values.

In fact, as mentioned above, water recirculates vertically at the eddy boundary during frontogenesis or symmetric instability, and EPV_x and EPV_z are key terms in semi-geostrophic frontogenesis (Hoskins & Bretherton, 1972).

Here we follow the Kushner and Shepherd (1995) approach to derive a semi-geostrophic Charney-Stern criterion for an isolated vortex on the $f-$ plane. Initially, we tried to adapt the Kushner and Shepherd (1995) theory in cylindrical coordinates by adding the cyclostrophic term to the equations. However, in polar coordinates, the radial and orthoradial velocity components are not independent due to the radius of curvature r. In particular, $v_\theta = r\dot{\theta}$ cannot be reduced to a generalized coordinate as in the Cartesian case because of this r dependence. As a consequence, further assumptions were necessary.

As in Section 5.1, consider an isolated but not necessarily axisymmetric eddy, at the surface of an infinite ocean. The radius of maximum velocity is denoted R and the generic velocity field takes the following form:

$$\vec{v}(r,\theta,z,t) = v_r(r,\theta,z,t)\vec{e_r} + v_\theta(r,\theta,z,t)\vec{e_\theta} + v_z(r,\theta,z,t)\vec{e_z} \tag{A1}$$

In cylindrical coordinates, the flow is governed by the following equations.

$$\frac{Dv_r}{Dt} - \left(f_0 + \frac{v_\theta}{r}\right)v_\theta = -f_0 v_\theta^g \tag{A2}$$

$$\frac{Dv_\theta}{Dt} + \left(f_0 + \frac{v_\theta}{r}\right)v_r = f_0 v_r^g \tag{A3}$$

$$\frac{1}{\rho_w}\frac{\partial p'}{\partial z} = b' \tag{A4}$$

$$\frac{1}{r}\frac{\partial (r v_r)}{\partial r} + \frac{1}{r}\frac{\partial v_\theta}{\partial \theta} + \frac{\partial v_z}{\partial z} = 0 \tag{A5}$$

$$\frac{Db'}{Dt} = 0 \tag{A6}$$

$$\frac{D}{Dt} = \frac{\partial}{\partial t} + v_r\frac{\partial}{\partial r} + v_\theta\frac{\partial}{r\partial\theta} + v_z\frac{\partial}{\partial z} \tag{A7}$$

where, v_r^g and v_θ^g are the geostrophic velocity respectively in the radial and orthoradial directions. As before, the prime denotes the buoyancy anomaly associated with the water mass trapped in the eddy core. Since instabilities develop locally and R is very large, we assume that the flow can be described in a local Cartesian frame near the eddy boundary (see Figure A1). Since we study small variations of r closed to R, we define the Cartesian variable $\varepsilon = r - R$ with $\varepsilon \ll R$. The curvature is locally neglected and we define the second Cartesian variable $y = R\theta$. Thus, we define the local Cartesian frame $\left(\vec{e}_\varepsilon, \vec{e}_y, \vec{e}_z\right)$ and the associated velocity field $\vec{v}(\varepsilon,y,z,t)$. We also define the rotational velocity $\Omega = \frac{v_\theta}{r}$ in the cylindrical system, which leads to $\Omega_R(\varepsilon, y, z, t)$ in the local Cartesian frame. Note that Ω_R is a regular function of ε, since it cannot diverge near the vortex center or at infinity. Then there exists a potential χ such that $\frac{d\chi}{d\varepsilon} = \Omega_R$. This will help us to define the generalized coordinates.

In this frame of reference, equations simply write:

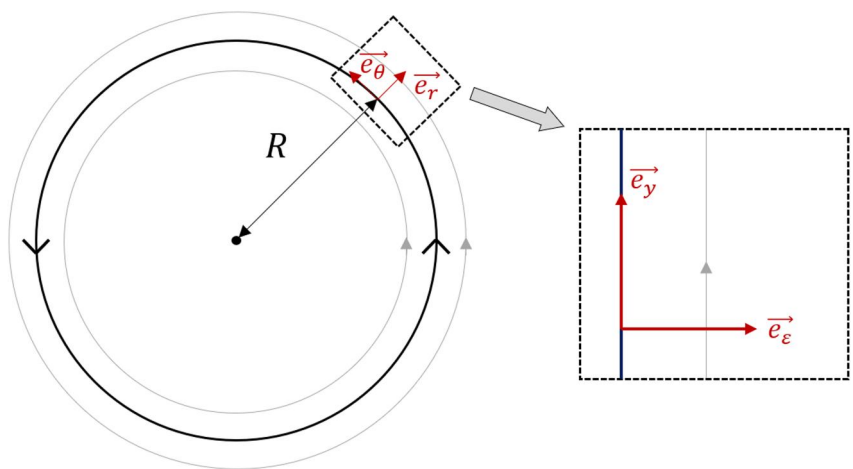

Figure A1. Local Cartesian frame at the eddy boundary. The curvature is locally neglected.

$$\frac{Dv_\varepsilon}{Dt} - \left(f_0 + \Omega_R\right) v_y = -f_0 v_y^g \tag{A8}$$

$$\frac{Dv_y}{Dt} + \left(f_0 + \Omega_R\right) v_\varepsilon = f_0 v_\varepsilon^g \tag{A9}$$

$$\frac{1}{\rho_w}\frac{\partial p'}{\partial z} = b' \tag{A10}$$

$$\frac{\partial v_\varepsilon}{\partial \varepsilon} + \frac{\partial v_y}{\partial y} + \frac{\partial v_z}{\partial z} = 0 \tag{A11}$$

$$\frac{Db'}{Dt} = 0 \tag{A12}$$

$$\frac{D}{Dt} = \frac{\partial}{\partial t} + v_\varepsilon \frac{\partial}{\partial \varepsilon} + v_y \frac{\partial}{\partial y} + v_z \frac{\partial}{\partial z} \tag{A13}$$

Note that this system has some peculiarities in that it retains the cyclostrophic terms, which are small but necessary for the global analysis.

Following Kushner and Shepherd (1995), we define the generalized coordinates, $T = t$, $E = \varepsilon + \frac{v_y}{f_0} + \frac{\chi}{f_0}$, $Y = y - \frac{v_\varepsilon}{f_0} + y\frac{\Omega_R^{(0)}}{f_0}$ and $Z = \frac{b'}{f_0^2}$ such that.

$$\frac{DY}{Dt} = v_y \tag{A14}$$

$$\frac{DE}{Dt} = v_\varepsilon \tag{A15}$$

$$\frac{DZ}{Dt} = 0 \tag{A16}$$

In fact, we replaced Ω_R with its constant value $\Omega_R^{(0)}$ at $\varepsilon = 0$ and at $t = 0$. When t is large, the variable Y is incomplete due to the cyclostrophic term, so we cannot obtain the desired form of the problem. To the best of our knowledge, there has never been a generalized system of quasi-Cartesian coordinates that corresponds to polar coordinates. This is a consequence of the presence of cyclostrophic terms. Even if our variable change is incomplete, it does not change the stability criterion. This is because in our Cartesian frame the basic flow is oriented according to $\vec{e_y}$. Then the Montgomery-Bernoulli potential for the local frame can be defined as a function of pressure p and velocities such that:

$$\Psi = \frac{p}{\rho_0} - f_0^2 Z z + \frac{1}{2}\left(v_\varepsilon^2 + v_y^2\right) \tag{A17}$$

which gives,

$$v_\varepsilon = -\frac{1}{f_0}\frac{\partial \Psi}{\partial Y} \tag{A18}$$

$$v_y = \frac{1}{f_0}\frac{\partial \Psi}{\partial E} \tag{A19}$$

The material derivative can also be expressed using these variables:

$$\frac{D}{DT} = \frac{D}{Dt} = \frac{\partial}{\partial T} - \frac{1}{f_0}\frac{\partial \Psi}{\partial Y}\frac{\partial}{\partial E} + \frac{1}{f_0}\frac{\partial \Psi}{\partial E}\frac{\partial}{\partial Y} \tag{A20}$$

Then, the Jacobian of the transformation is proportional to the Ertel Potential vorticity q of the flow:

$$q \propto \frac{\partial(E,Y,Z)}{\partial(\varepsilon,y,z)} \tag{A21}$$

For a frontal vortex, we use the inverse of this quantity to avoid isopycnal pinching. We denote this quantity as $\sigma = \frac{1}{q}$. We assume that the vortex is isolated and that the flow is inviscid, incompressible and without forcing. Under these conditions σ is conserved:

$$\frac{D\sigma}{Dt} = 0 \tag{A22}$$

From the linearized equations of motion, we now derive the linear Charney-Stern theorem for small perturbations of the corresponding steady state. We linearize the motion around the rotating flow, which becomes a meridional steady state $\overline{v_y}(\varepsilon)$. In the initial state $\partial_\varepsilon = 0$, and thus $\partial_E = 0$. The velocity field has the following form:

$$\vec{v}(\varepsilon,y,z,t) = v'_\varepsilon(\varepsilon,y,z,t)\vec{e_\varepsilon} + \left(\overline{v_y}(y,z) + v'_y(\varepsilon,y,z,t)\right)\vec{e_y} + v'_z(\varepsilon,y,z,t)\vec{e_z} \tag{A23}$$

Now the problem is similar to that of Kushner and Shepherd (1995). By neglecting the boundary terms, the pseudo momentum equation can be written as follows:

$$\frac{\partial}{\partial t}\int_D \left(\frac{\sigma'^2}{2\overline{\sigma}\frac{\partial\overline{\sigma}}{\partial_E}}\right) dD = 0 \tag{A24}$$

where D is the infinite space. Denoting $\langle\cdot\rangle$ the average on the $\vec{e_y}$ direction, the equation takes the following form:

$$\frac{\partial}{\partial t}\iint \left(\frac{\langle\sigma'^2\rangle}{2\overline{\sigma}\frac{\partial\overline{\sigma}}{\partial_E}}\right) d\varepsilon dz = 0 \tag{A25}$$

As a result, the quantity $\overline{\sigma}\frac{\partial\overline{\sigma}}{\partial E}$ must change its sign and vanish in order for instability to occur. Considering this:

$$\overline{\sigma} = \frac{1}{\overline{q}} \tag{A26}$$

$$\frac{\partial\overline{\sigma}}{\partial E} = \frac{\partial\overline{\sigma}}{\partial\varepsilon}\frac{\partial\varepsilon}{\partial E} \tag{A27}$$

We obtain:

$$\frac{\partial\overline{\sigma}}{\partial E} = -\frac{\overline{q}}{\overline{q}^4}\frac{\partial\overline{q}}{\partial\varepsilon}\frac{\partial\varepsilon}{\partial E} \tag{A28}$$

Therefore, the quantity $\overline{q}\frac{\partial\overline{q}}{\partial\varepsilon}\frac{\partial E}{\partial\varepsilon}$ must change sign for an instability to grow. This necessary condition for instability gathers three conditions:

- If $\overline{q}\frac{\partial\overline{q}}{\partial\varepsilon}$ retains its sign, then $\frac{\partial E}{\partial\varepsilon} = \omega_a/f_0$, where ω_a is the absolute vorticity, must change sign. We recover the necessary condition for the anticyclonic ageostrophic instability (McWilliams et al., 2004);
- If $\frac{\partial\overline{q}}{\partial\varepsilon}\frac{\partial E}{\partial\varepsilon}$ retains its sign, then q must change its sign, and as a consequence the Ertel potential vorticity must change its sign. We recover the necessary condition for symmetric instability with $f_0 > 0$ (Fjørtoft, 1950).

- Finally, if $\overline{q}$ maintains its sign, then $\frac{\partial \overline{q}}{\partial \varepsilon}\frac{\partial E}{\partial \varepsilon}$ must change sign, which is the necessary condition for inertial instability (Eliassen, 1983). In fact, $\frac{\partial \overline{q}}{\partial \varepsilon}$ represents the angular momentum and $\frac{\partial E}{\partial \varepsilon}$ its derivative with respect to ε.

The second condition gives us a constraint on the α values. The regions in which the Ertel potential vorticity becomes negative correspond to the regions in which $\alpha > 1$. Therefore, from this theoretical necessary condition, we expect $\alpha < 1$ for a large part of the vortex boundary. This statement is consistent with Figure 10, which shows that α is less than 1 for almost 100% of the eddy boundary area.

Data Availability Statement

In this study, we benefited from numerous data sets freely available and listed here. The concatenated RVs Atalante and Maria S Merian hydrographic and velocity data (L'Hegaret Pierre & Sabrina., 2020) are freely available on the SEANOE website: https://www.seanoe.org/data/00809/92071/, accessed on 15 March 2021.

The hydrographic and velocity measurements taken during the M124 cruise (Karstensen & Krahmann, 2016; Karstensen, Speich, et al., 2016; Karstensen & Wölfl, 2016) of the RV Meteor are freely available on the PANGAEA web site: https://doi.org/10.1594/PANGAEA.902947, https://doi.pangaea.de/10.1594/PANGAEA.863015, https://doi.pangaea.de/10.1594/PANGAEA.869740.

The hydrographic and velocity data collected during the M160 cruise (Dengler et al., 2022a, 2022b; Dengler, Fischer, et al., 2022) of the RV Meteor are freely available on the PANGAEA web site: https://doi.org/10.1594/PANGAEA.943409, https://doi.org/10.1594/PANGAEA.943432, https://doi.org/10.1594/PANGAEA.943657.

Finally, hydrographic and velocity data collected during the RV Kristine Bonnevie KB2017606 cruise (Fer et al., 2019) are freely available on the NMDC website: https://doi.org/10.21335/NMDC-1093031037.

Acknowledgments
This research has been supported by the European Union Horizon2020 research and innovation program under Grant 817578 (TRIATLAS), the Centre National d'Etudes Spatiales through the TOEddies and EUREC4A-OA projects, the French national programme LEFE INSU, IFREMER, the French vessel research fleet, the French research infrastructures AERIS and ODATIS, IPSL, the Chaire Chanel programme of the Geosciences Department at ENS, and the EUREC4A-OA JPI Ocean and Climate programme. We would also like to thank the captains, crews and scientists of the RVs Atalante, Maria S. Merian, Meteor and Kristine Bonnevie. Yan Barabinot is supported by a Ph.D grant from Ecole Normale Supérieure de Saclay. Xavier Carton acknowledges support by UBO and by a CNES contract EUREC4A-OA.

References

Archer, M. R., Schaeffer, A., Keating, S. R., Roughan, M., Holmes, R. M., & Siegelman, L. (2020). Observations of submesoscale variability and frontal subduction within the mesoscale eddy field of the Tasman Sea. *Journal of Physical Oceanography*, *50*(5), 1509–1529. https://doi.org/10.1175/jpo-d-19-0131.1

Barceló-Llull, B., Sangrà, P., Pallàs-Sanz, E., Barton, E. D., Estrada-Allis, S., Martínez-Marrero, A., et al. (2017). Anatomy of a subtropical intrathermocline eddy.

Barkan, R., Srinivasan, K., Yang, L., McWilliams, J. C., Gula, J., & Vic, C. (2021). Oceanic mesoscale eddy depletion catalyzed by internal waves. *Geophysical Research Letters*, *48*(18), e2021GL094376. https://doi.org/10.1029/2021gl094376

Bashmachnikov, I. L., & Carton, X. (2012). Surface signature of mediterranean water eddies in the northeastern Atlantic: Effect of the upper ocean stratification. *Ocean Science*, *8*(6), 931–943. https://doi.org/10.5194/os-8-931-2012

Benthuysen, J. A., & Thomas, L. N. (2012). Friction and diapycnal mixing at a slope: Boundary control of potential vorticity. *Journal of Physical Oceanography*, *42*(9), 1509–1523. https://doi.org/10.1175/jpo-d-11-0130.1

Beron-Vera, F. J., Wang, Y., Olascoaga, M. J., Goñi, G., & Haller, G. (2013). Objective detection of oceanic eddies and the agulhas leakage. *Journal of Physical Oceanography*, *43*(7), 1426–1438. https://doi.org/10.1175/jpo-d-12-0171.1

Bosse, A., Fer, I., Lilly, J. M., & Søiland, H. (2019). Dynamical controls on the longevity of a non-linear vortex: The case of the lofoten basin eddy. *Scientific Reports*, *9*, 202580306. https://doi.org/10.1038/s41598-019-49599-8

Bowden, K. F. (1965). Horizontal mixing in the sea due to a shearing current. *Journal of Fluid Mechanics*, *21*(01), 83–95. https://doi.org/10.1017/s0022112065000058

Bryden, H. L. (1979). Poleward heat flux and conversion of available potential energy in drake passage. *Journal of Marine Research*, *37*, 1–12.

Buckingham, C. E., Gula, J., & Carton, X. (2021). The role of curvature in modifying frontal instabilities. Part I: Review of theory and presentation of a nondimensional instability criterion. *Journal of Physical Oceanography*, *51*(2), 299–315. https://doi.org/10.1175/jpo-d-19-0265.1

Bulters, A. C. (2012). Three-dimensional structure of thermohaline staircases in the tropical north Atlantic and their effect on acoustic propagation.

Carton, X., Flierl, G. R., & Polvani, L. M. (1989). The generation of tripoles from unstable axisymmetric isolated vortex structures. *Europhysics Letters*, *9*(4), 339–344. https://doi.org/10.1209/0295-5075/9/4/007

Chaigneau, A., Eldin, G., & Dewitte, B. (2009). Eddy activity in the four major upwelling systems from satellite altimetry (1992-2007). *Progress in Oceanography*, *83*(1–4), 117–123. https://doi.org/10.1016/j.pocean.2009.07.012

Chelton, D., Schlax, M. G., & Samelson, R. M. (2011). Global observations of nonlinear mesoscale eddies. *Progress in Oceanography*, *91*(2), 167–216. https://doi.org/10.1016/j.pocean.2011.01.002

Chen, J., Tapley, B. D., Wilson, C. R., Cazenave, A., Seo, K., & Kim, J. (2020). Global ocean mass change from grace and grace follow-on and altimeter and argo measurements. *Geophysical Research Letters*, *47*(22). https://doi.org/10.1029/2020gl090656

Chen, Y., Speich, S., & Laremxenaire, R. (2021). Formation and transport of the south Atlantic subtropical mode water in eddy-permitting observations. *Journal of Geophysical Research: Oceans*, *127*(1). https://doi.org/10.1029/2021jc017767

D'Addezio, J. M., Bingham, F. M., & Jacobs, G. A. (2019). *Sea surface salinity subfootprint variability estimates from regional high-resolution model simulations*. Remote Sensing of Environment.

De Marez, C., Meunier, T., Morvan, M., L'Hégaret, P., & Carton, X. (2020). Study of the stability of a large realistic cyclonic eddy. *Ocean Modelling*, *146*, 101540. https://doi.org/10.1016/j.ocemod.2019.101540

Dengler, M., Fischer, T., Körtzinger, A., & Krahmann, G. (2022). ADCP current measurements (38 and 75 kHz) during METEOR cruise M160 (data set). *PANGAEA*. https://doi.org/10.1594/PANGAEA.943409

Dengler, M., Körtzinger, A., & Krahmann, G. (2022a). Physical oceanography (CTD) during METEOR cruise M160 (data set). *PANGAEA*. https://doi.org/10.1594/PANGAEA.943432

Dengler, M., Körtzinger, A., & Krahmann, G. (2022b). Underway CTD data collected during METEOR cruise M160 (data set). *PANGAEA*. https://doi.org/10.1594/PANGAEA.943657

Egger, J., & Chaudhry, Q. Z. (2009). Progress of research on potential vorticity and its inversion.

Eliassen, A. (1983). The charney-stern theorem on barotropic-baroclinic instability. *Pure and Applied Geophysics*, *121*(3), 563–572. https://doi.org/10.1007/bf02590155

Ertel, H. (1942). Ein neuer hydrodynamischer erhaltungssatz. *Naturwissenschaften*, *30*(36), 543–544. https://doi.org/10.1007/bf01475602

Fer, I., Bosse, A., Søiland, H., Ferron, B., & Bouruet-Aubertot, P. (2019). Ocean currents, hydrography and microstructure data from provolo cruises (data set). *NMDC*. https://doi.org/10.21335/NMDC-1093031037

Fer, I., Voet, G., Seim, K. S., Rudels, B., & Latarius, K. (2010). Intense mixing of the faroe bank channel overflow. *Geophysical Research Letters*, *37*(2), L02604. https://doi.org/10.1029/2009gl041924

Fjørtoft, R. (1950). Application of integral theorems in deriving criteria of stability for laminar flows and for the baroclinic circular vortex.

Flierl, G. R. (1981). Particle motions in large-amplitude wave fields. *Geophysical & Astrophysical Fluid Dynamics*, *18*(1–2), 39–74. https://doi.org/10.1080/03091928108208773

Frenger, I., Gruber, N., Knutti, R., & Münnich, M. (2013). Imprint of southern ocean eddies on winds, clouds and rainfall. *Nature Geoscience*, *6*(8), 608–612. https://doi.org/10.1038/ngeo1863

Halle, C., & Pinkel, R. (2003). Internal wave variability in the Beaufort Sea during the winter of 1993/1994. *Journal of Geophysical Research*, *108*(C7), 3210. https://doi.org/10.1029/2000jc000703

Hoskins, B. J. (1974). The role of potential vorticity in symmetric stability and instability. *Quarterly Journal of the Royal Meteorological Society*, *100*(425), 480–482. https://doi.org/10.1256/smsqj.42519

Hoskins, B. J. (1982). The mathematical theory of frontogenesis. *Annual Review of Fluid Mechanics*, *14*(1), 131–151. https://doi.org/10.1146/annurev.fl.14.010182.001023

Hoskins, B. J., & Bretherton, F. P. (1972). Atmospheric frontogenesis models: Mathematical formulation and solution. *Journal of the Atmospheric Sciences*, *29*(1), 11–37. https://doi.org/10.1175/1520-0469(1972)029<0011:afmmfa>2.0.co;2

Hua, B. L., & Klein, P. (1998). An exact criterion for the stirring properties of nearly two-dimensional turbulence. *Physica D: Nonlinear Phenomena*, *113*(1), 98–110. https://doi.org/10.1016/s0167-2789(97)00143-7

Hunt, J. C. R., Leibovich, S., & Richards, K. J. (1988). Turbulent shear flows over low hills. *Quarterly Journal of the Royal Meteorological Society*, *114*(484), 1435–1470. https://doi.org/10.1256/smsqj.48404

Ienna, F., Bashmachnikov, I., & Dias, J. (2022). Meddies and their sea surface expressions: Observations and theory. *Journal of Physical Oceanography*, *52*(11), 2643–2656. https://doi.org/10.1175/JPO-D-22-0081.1

Ioannou, A., Speich, S., & Laxenaire, R. (2022). Characterizing mesoscale eddies of eastern upwelling origins in the Atlantic Ocean and their role in offshore transport. *Frontiers in Marine Science*, *9*. https://doi.org/10.3389/fmars.2022.835260

Jayne, S. R., & Marotzke, J. (2002). The oceanic eddy heat transport. *Journal of Physical Oceanography*, *32*(12), 3328–3345. https://doi.org/10.1175/1520-0485(2002)032<3328:toeht>2.0.co;2

Joyce, T. M. (1977). A note on the lateral mixing of water masses. *Journal of Physical Oceanography*, *7*(4), 626–629. https://doi.org/10.1175/1520-0485(1977)007<0626:anotlm>2.0.co;2

Joyce, T. M. (1984). Velocity and hydrographic structure of a gulf stream warm-core ring. *Journal of Physical Oceanography*, *14*(5), 936–947. https://doi.org/10.1175/1520-0485(1984)014<0936:vahsoa>2.0.co;2

Karstensen, J., & Krahmann, G. (2016). Physical oceanography during METEOR cruise M124 (data set). *PANGAEA*. https://doi.org/10.1594/PANGAEA.863015

Karstensen, J., Sabrina, S., Raphael, M., Karl, B., Jennifer, C., Marco, G., et al. (2016). Oceanic & atmospheric variability in the south Atlantic. cruise no. m124. *PANGAEA*, M124. https://doi.org/10.1594/PANGAEA.869740

Karstensen, J., Speich, S., Morard, R., Bumke, K., Clarke, J., Giorgetta, M., et al. (2016). Oceanic & atmospheric variability in the south Atlantic cruise no. m124 29. february–18. march 2016 cape town (republic South Africa)–rio de janeiro (Brazil).

Karstensen, J., & Wölfl, A.-C. (2016). Raw multibeam EM122 data: METEOR cruise M124 (SE Atlantic) (data set). *PANGAEA*. https://doi.org/10.1594/PANGAEA.869740

Katz, E. J. (1969). Further study of a front in the Sargasso Sea. *Tellus*, *21*(2), 259–269. https://doi.org/10.1111/j.2153-3490.1969.tb00437.x

Körtzinger, A., & Team, E. S. (2021). Meteor m160 cruise report, 19 January - 19 February 2020. *PANGAEA*. https://doi.org/10.1594/PANGAEA.943432

Kushner, P. J., & Shepherd, T. G. (1995). Wave-activity conservation laws and stability theorems for semi-geostrophic dynamics. part 2. pseudoenergy-based theory. *Journal of Fluid Mechanics*, *290*, 105–129. https://doi.org/10.1017/s0022112095002436

Lapeyre, G., Hua, B. L., & Klein, P. (2001). Dynamics of the orientation of active and passive scalars in two-dimensional turbulence. *Physics of Fluids*, *13*(1), 251–264. https://doi.org/10.1063/1.1324705

Large, W. G., McWilliams, J. C., & Doney, S. C. (1994). Oceanic vertical mixing: A review and a model with a nonlocal boundary layer parameterization. *Oceanographic Literature Review*, *7*(4), 363–403. https://doi.org/10.1029/94rg01872

Laxenaire, R., Speich, S., Blanke, B., Chaigneau, A., Pegliasco, C., & Stegner, A. (2018). Anticyclonic eddies connecting the western boundaries of Indian and Atlantic oceans. *Journal of Geophysical Research: Oceans*, *123*(11), 7651–7677. https://doi.org/10.1029/2018jc014270

Laxenaire, R., Speich, S., & Stegner, A. (2019). Evolution of the thermohaline structure of one agulhas ring reconstructed from satellite altimetry and argo floats. *Journal of Geophysical Research*, *124*(12), 8969–9003. https://doi.org/10.1029/2018jc014426

Laxenaire, R., Speich, S., & Stegner, A. (2020). Agulhas ring heat content and transport in the south Atlantic estimated by combining satellite altimetry and argo profiling floats data. *Journal of Geophysical Research*, *125*(9). https://doi.org/10.1029/2019jc015511

Legras, B., & Dritschel, D. G. (1993). Vortex stripping and the generation of high vorticity gradients in two-dimensional flows. *Flow, Turbulence and Combustion*, *51*(1–2), 445–455. https://doi.org/10.1007/bf01082574

L'Hégaret, P., Carton, X., Louazel, S., & Boutin, G. (2015). Mesoscale eddies and submesoscale structures of Persian gulf water off the Omani coast in spring 2011. *Ocean Science*, *12*(3), 687–701. https://doi.org/10.5194/os-12-687-2016

L'Hégaret, P., Duarte, R., Carton, X., Vic, C., Ciani, D., Baraille, R., & Corréard, S. (2015). Mesoscale variability in the Arabian Sea from hycom model results and observations: Impact on the Persian gulf water path. *Ocean Science*, *11*(5), 667–693. https://doi.org/10.5194/os-11-667-2015

L'Hégaret, P., Schütte, F., Speich, S., Reverdin, G., Baranowski, D. B., Czeschel, R., et al. (2022). Ocean cross-validated observations from the r/vs l'atalante, maria s. merian and meteor and related platforms as part of the eurec 4 a-oa/atomic campaign. *Earth System Science Data Discussions*, *1–39*.

L'Hegaret Pierre, K. J., & Sabrina, S. (2020). Concatenated temperature, salinity, and velocity measurements from eurec4a_oa/atomic ctd, uctd, mvpands – adcpdatafromther/vsl′atalanteandmarias.merian. Retrieved from https://www.seanoe.org/data/00809/92071

Li, C., Zhang, Z., Zhao, W., & Tian, J. (2017). A statistical study on the subthermocline submesoscale eddies in the northwestern Pacific Ocean based on argo data. *Journal of Geophysical Research: Oceans*, *122*(5), 3586–3598. https://doi.org/10.1002/2016jc012561

Lozier, M. S. (1997). Evidence for large-scale eddy-driven gyres in the north Atlantic. *Science*, *277*(5324), 361–364. https://doi.org/10.1126/science.277.5324.361

Lumpkin, R. (2016). Global characteristics of coherent vortices from surface drifter trajectories. *Journal of Geophysical Research*, *121*(2), 1306–1321. https://doi.org/10.1002/2015jc011435

Mariotti, A., Legras, B., & Dritschel, D. G. (1994). Vortex stripping and the erosion of coherent structures in two-dimensional flows. *Physics of Fluids*, *6*(12), 3954–3962. https://doi.org/10.1063/1.868385

Marshall, J., & Schott, F. A. (1999). Open-ocean convection: Observations, theory, and models. *Reviews of Geophysics*, *37*, 1–64. https://doi.org/10.1029/98rg02739

Marshall, J., & Speer, K. (2012). Closure of the meridional overturning circulation through southern ocean upwelling. *Nature Geoscience*, *5*(3), 171–180. https://doi.org/10.1038/ngeo1391

Martin, A. P., Richards, K. J., Bracco, A., & Provenzale, A. (2002). Patchy productivity in the open ocean. *Global Biogeochemical Cycles*, *16*(2). https://doi.org/10.1029/2001gb001449

McWilliams, J. C., Molemaker, M., & Yavneh, I. (2004). Ageostrophic, anticyclonic instability of a geostrophic, barotropic boundary current. *Physics of Fluids*, *16*(10), 3720–3725. https://doi.org/10.1063/1.1785132

Monin, A., & Yaglom, A. (1971). *Statistical fluid mechanics* (Vol. 2). MIT Press.

Morel, Y., Gula, J., & Ponte, A. L. (2019). Potential vorticity diagnostics based on balances between volume integral and boundary conditions. *Ocean Modelling*, *138*, 23–35. https://doi.org/10.1016/j.ocemod.2019.04.004

Morrow, R., Coleman, R., Church, J. A., & Chelton, D. (1994). Surface eddy momentum flux and velocity variances in the southern ocean from geosat altimetry. *Journal of Physical Oceanography*, *24*(10), 2050–2071. https://doi.org/10.1175/1520-0485(1994)024<2050:semfav>2.0.co;2

Morrow, R., & Traon, P.-Y. L. (2012). Recent advances in observing mesoscale ocean dynamics with satellite altimetry. *Advances in Space Research*, *50*(8), 1062–1076. https://doi.org/10.1016/j.asr.2011.09.033

Morvan, M., L'Hégaret, P., Carton, X., Gula, J., Vic, C., De Marez, C., et al. (2019). The life cycle of submesoscale eddies generated by topographic interactions. *Ocean Science*, *15*(6), 1531–1543. https://doi.org/10.5194/os-15-1531-2019

Nencioli, F., d'Ovidio, F., Doglioli, A. M., & Petrenko, A. A. (2013). In situ estimates of submesoscale horizontal eddy diffusivity across an ocean front. *Journal of Geophysical Research: Oceans*, *118*(12), 7066–7080. https://doi.org/10.1002/2013jc009252

Nencioli, F., Kuwahara, V. S., Dickey, T. D., Rii, Y. M., & Bidigare, R. R. (2008). Physical dynamics and biological implications of a mesoscale eddy in the lee of Hawai'i: Cyclone opal observations during e-flux iii. *Deep-sea Research Part II-Topical Studies in Oceanography*, *55*(10–13), 1252–1274. https://doi.org/10.1016/j.dsr2.2008.02.003

Nencioli, F., Nencioli, F., Petrenko, A. A., & Doglioli, A. M. (2016). Diagnosing cross-shelf transport along an ocean front: An observational case study in the gulf of lion. *Journal of Geophysical Research*, *121*(10), 7218–7243. https://doi.org/10.1002/2016jc011908

Okubo, A. (1970). Horizontal dispersion of floatable particles in the vicinity of velocity singularities such as convergences. *Deep Sea Research and Oceanographic Abstracts*, *17*(3), 445–454. https://doi.org/10.1016/0011-7471(70)90059-8

Pacanowski, R. C., & Philander, S. G. (1981). Parameterization of vertical mixing in numerical models of tropical oceans. *Journal of Physical Oceanography*, *11*, 1443–1451. https://doi.org/10.1175/1520-0485(1981)011<1443:povmin>2.0.co;2

Paillet, J., Cann, B. L., Carton, X., Morel, Y., & Serpette, A. (2002). Dynamics and evolution of a northern meddy. *Journal of Physical Oceanography*, *32*(1), 55–79. https://doi.org/10.1175/1520-0485(2002)032<0055:daeoan>2.0.co;2

Peliz, A., Boutov, D., Aguiar, A. C. B., & Carton, X. (2014). The gulf of cadiz gap wind anticyclones. *Continental Shelf Research*, *91*, 171–191. https://doi.org/10.1016/j.csr.2014.09.004

Peters, H., Gregg, M., & Toole, J. (1988). On the parameterization of equatorial turbulence. *Journal of Geophysical Research*, *93*(C2), 1199–1218. https://doi.org/10.1029/jc093ic02p01199

Pinot, J. M., Tintoré, J., Lopezjurado, J., Depuelles, M., & Jansa, J. (1995). Three-dimensional circulation of a mesoscale eddy/front system and its biological implications. *Oceanologica Acta*, *18*, 389–400.

Rhines, P. B. (1975). Waves and turbulence on a beta-plane. *Journal of Fluid Mechanics*, *69*(3), 417–443. https://doi.org/10.1017/s0022112075001504

Richardson, P. L., & Tychensky, A. (1998). Meddy trajectories in the canary basin measured during the semaphore experiment, 1993–1995. *Journal of Geophysical Research*, *103*(C11), 25029–25045. https://doi.org/10.1029/97jc02579

Ruddick, B. R., & Gargett, A. E. (2003). Oceanic double-diffusion: Introduction [progress in oceanography 56 (2003) 381–393]. *Progress in Oceanography*, *57*(2), 237. https://doi.org/10.1016/s0079-6611(03)00086-7

Ruddick, B. R., Oakey, N. S., & Hebert, D. (2010). Measuring lateral heat flux across a thermohaline front: A model and observational test. *Journal of Marine Research*, *68*(3), 523–539. https://doi.org/10.1357/002224010794657146

Rudnick, D. L. (2001). On the skewness of vorticity in the upper ocean. *Geophysical Research Letters*, *28*(10), 2045–2048. https://doi.org/10.1029/2000gl012265

Sallée, J., Speer, K., Rintoul, S. R., & Wijffels, S. E. (2010). Southern ocean thermocline ventilation. *Journal of Physical Oceanography*, *40*(3), 509–529. https://doi.org/10.1175/2009jpo4291.1

Shcherbina, A. Y., D'Asaro, E. A., Lee, C. M., Klymak, J. M., Molemaker, M., & McWilliams, J. C. (2013). Statistics of vertical vorticity, divergence, and strain in a developed submesoscale turbulence field. *Geophysical Research Letters*, *40*(17), 4706–4711. https://doi.org/10.1002/grl.50919

Shi, Q., & Wang, G. (2020). Observed warm filaments from the kuroshio associated with mesoscale eddies. *Remote Sensing*, *12*(18), 3090. https://doi.org/10.3390/rs12183090

Smith, W. H. F., & Sandwell, D. T. (1997). Global sea floor topography from satellite altimetry and ship depth soundings. *Science*, *277*(5334), 1956–1962. https://doi.org/10.1126/science.277.5334.1956

Snyder, C., Muraki, D. J., Plougonven, R., & Zhang, F. (2007). Inertia–gravity waves generated within a dipole vortex. *Journal of the Atmospheric Sciences*, *64*(12), 4417–4431. https://doi.org/10.1175/2007jas2351.1

Sobel, A. H., Plumb, R. A., & Waugh, D. W. (1997). Methods of calculating transport across the polar vortex edge. *Journal of the Atmospheric Sciences*, *54*(18), 2241–2260. https://doi.org/10.1175/1520-0469(1997)054<2241:moctat>2.0.co;2

Søiland, H., & Team, E. S. (2017). Cruise kb 2017606 with r.v. kristine bonnevie. *PANGAEA*. https://doi.org/10.1594/PANGAEA.943432

Speich, S., & Team, E. S. (2021). Eurec4a-oa cruise report, 19 January - 19 February 2020, vessel: L'atalante. *ARCHIMER Ifremer's Institutional Repository*. https://doi.org/10.13155/80129

Stegner, A., & Dritschel, D. G. (2000). A numerical investigation of the stability of isolated shallow water vortices. *Journal of Physical Oceanography*, *30*(10), 2562–2573. https://doi.org/10.1175/1520-0485(2000)030<2562:aniots>2.0.co;2

Stevens, B., Bony, S., Farrell, D., Ament, F., Blyth, A., Fairall, C., et al. (2021). Eurec^{4}a. *Earth System Science Data*, *13*(8), 4067–4119. https://doi.org/10.5194/essd-13-4067-2021

Subirade, C., L'Hégaret, P., Speich, S., Laxenaire, R., Karstensen, J., & Carton, X. (2023). Combining an eddy detection algorithm with in-situ measurements to study north Brazil current rings. *Remote Sensing*, *15*(7), 1897. https://doi.org/10.3390/rs15071897

Sun, W., An, M., Liu, J., Liu, J., Yang, J., Tan, W., et al. (2022). Comparative analysis of four types of mesoscale eddies in the kuroshio-oyashio extension region. *Frontiers in Marine Science*, *9*, 984244. https://doi.org/10.3389/fmars.2022.984244

Thomas, L. N., Taylor, J. R., Ferrari, R., & Joyce, T. M. (2013). Symmetric instability in the Gulf stream. *Deep-sea Research Part II: Topical Studies in Oceanography*, *91*, 96–110. https://doi.org/10.1016/j.dsr2.2013.02.025

Thorpe, S. A. (2005). The turbulent ocean.

Toole, J. M., & Schmitt, R. W. (1987). Small-scale structures in the north-west Atlantic sub-tropical front. *Nature*, *327*(6117), 47–49. https://doi.org/10.1038/327047a0

Turner, J. S. (1973). Buoyancy effects in fluids.

Voorhis, A. D., & Hersey, J. (1964). Oceanic thermal fronts in the Sargasso Sea. *Journal of Geophysical Research*, *69*(18), 3809–3814. https://doi.org/10.1029/jz069i018p03809

Weiss, J. (1991a). The dynamics of enstrophy transfer in two-dimensional hydrodynamics. *Physica D: Nonlinear Phenomena*, *48*(2–3), 273–294. https://doi.org/10.1016/0167-2789(91)90088-q

Weiss, J. (1991b). The dynamics of entropy transfer in two-dimensional hydrodynamics. *Physica D: Nonlinear Phenomena*, *48*(2–3), 273–294. https://doi.org/10.1016/0167-2789(91)90088-q

Welander, P. (1973). Lateral friction in the oceans as an effect of potential vorticity mixing. *Geophysical & Astrophysical Fluid Dynamics*, *5*(1), 173–189. https://doi.org/10.1080/03091927308236114

Wunsch, C. (1999). Where do ocean eddy heat fluxes matter. *Journal of Geophysical Research*, *104*(C6), 13235–13249. https://doi.org/10.1029/1999jc900062

Yu, Z., & Schopf, P. S. (1997). Vertical eddy mixing in the tropical upper ocean: Its influence on zonal currents. *Journal of Physical Oceanography*, *27*(7), 1447–1458. https://doi.org/10.1175/1520-0485(1997)027<1447:vemitt>2.0.co;2

Zaron, E. D., & Moum, J. N. (2009). A new look at richardson number mixing schemes for equatorial ocean modeling. *Journal of Physical Oceanography*, *39*(10), 2652–2664. https://doi.org/10.1175/2009jpo4133.1

Zhang, Y., Wu, G., Liu, Y., & Guan, Y. (2014). The effects of asymmetric potential vorticity forcing on the instability of south Asia high and Indian summer monsoon onset. *Science China Earth Sciences*, *57*(2), 337–350. https://doi.org/10.1007/s11430-013-4664-8

Zhang, Z., Tian, J., Qiu, B., Zhao, W., Chang, P., Wu, D., & Wan, X. (2016). Observed 3d structure, generation, and dissipation of oceanic mesoscale eddies in the south China Sea. *Scientific Reports*, *6*(1), 24349. https://doi.org/10.1038/srep24349

Zhang, Z., Zhang, X., Qiu, B., Zhao, W., Zhou, C., Huang, X., & Tian, J. (2021). Submesoscale currents in the subtropical upper ocean observed by long-term high-resolution mooring arrays. *Journal of Physical Oceanography*, *51*(1), 187–206. https://doi.org/10.1175/jpo-d-20-0100.1